actuators

MDPI

Article

A Novel Low-Complexity Cascaded Model Predictive Control Method for PMSM

Qingcheng Meng [1] and Guangqing Bao [2,*]

[1] College of Electrical and Information Engineering, Lanzhou University of Technology, Lanzhou 730050, China; mqc0460@163.com
[2] School of Electrical Engineering and Information, Southwest Petroleum University, Chengdu 610500, China
* Correspondence: baogq03@163.com

Abstract: A novel low-complexity cascaded model predictive control method for permanent magnet synchronous motors is proposed to achieve a fast dynamic response to ensure the system's steady-state performance. Firstly, a predictive speed controller based on an extended state observer is designed in the outer speed loop to improve the anti-interference ability of the system; then, a low-complexity three-vector predictive control algorithm is adopted in the current inner loop, taking into account the steady-state performance of the system and lower computational burden. Finally, a comparative analysis is conducted between the proposed method and traditional methods through simulation and experiments, proving that the proposed method performs well in dynamic and static performance. On this basis, the computational complexity of the current inner loop three-vector prediction algorithm is effectively reduced, indicating the correctness and effectiveness of the proposed method.

Keywords: model predictive control; cascaded method; permanent magnet synchronous motor (PMSM)

check for updates

Citation: Meng, Q.; Bao, G. A Novel Low-Complexity Cascaded Model Predictive Control Method for PMSM. *Actuators* **2023**, *12*, 349. https://doi.org/10.3390/act12090349

Received: 18 July 2023
Revised: 28 August 2023
Accepted: 28 August 2023
Published: 31 August 2023

1. Introduction

In recent years, permanent magnet synchronous motors (PMSMs) have high efficiency, high power density, and good structural reliability [1], and have been widely used in power transmission fields such as wind power generation [2], robotics [3], electric vehicles [4], and numerically controlled machine tools [5].

At the same time, higher requirements are also put forward for its control performance. If the traditional PI controller is still used for the speed loop, its response speed and anti-interference ability cannot meet the requirements. To solve this problem, some scholars have proposed adaptive control [6], fuzzy control [7], sliding mode control [8], model predictive control (MPC) [9], etc. Adaptive control has the disadvantage of local convergence in solving problems for the above algorithms. Fuzzy control algorithms cause excessive controller computation, while sliding mode control has stability and inherent chattering problems. In contrast, MPC has a more concise control idea, can better deal with nonlinear constraints and achieve multi-objective optimization, and has superior dynamic performance. The authors of [9] designed a predictive controller in the speed loop and introduced a high-order sliding mode disturbance observer to ensure the system has both fast dynamic response performance and good robustness. The final simulation and experimental results verified the effectiveness of the proposed method. However, the parameter design and stability proof of the high-order terminal sliding mode disturbance observer are very complex, limiting its further application in practical systems.

In addition, a high-performance AC motor drive also puts forward higher requirements for the current loop [10]. Although the traditional field-oriented control (FOC) has good steady-state performance, its control process involves tuning multiple controller parameters, which is relatively complex [11], and the bandwidth of the internal current

loop limits its dynamic characteristics. Direct torque control (DTC) outputs a control signal through a hysteresis comparator, which has good dynamic performance, but has the disadvantage of large torque ripple and current ripple, and its overall steady-state performance is poor [12], so it is not suitable for high-performance control occasions. The current loop applies MPC, which solves the problems in the traditional FOC and DTC methods. Because of its more flexible control idea, it can better balance the dynamic and steady-state performance [13], and does not need complex control parameter tuning.

For the current loop, the traditional MPC algorithm only acts on one voltage vector in a sampling period, which makes it have the disadvantages of poor system steady-state performance and an unfixed switching frequency [14]. The intuitive solution to this problem is to shorten the size of the sampling cycle, but this comes with high requirements for the system's hardware circuit. Therefore, improving the steady-state performance of the system without increasing the sampling frequency is worth studying [15], and had led to the proposal by some scholars to apply multiple voltage vectors within a sampling period.

In this regard, some scholars proposed combining the active voltage vector and the zero-voltage vector. Within a sampling period, the active voltage vector only acts for a portion of the time, and the remaining time is affected by the zero-voltage vector [16]. However, this voltage vector combination can only change the amplitude of the active voltage vector and cannot change the direction of the voltage vector, resulting in a limited current ripple suppression effect. To adjust the voltage amplitude and direction, the authors of [17] proposed a generalized dual-vector method for induction motors, which expands the dual-vector combination to any combination between two primary voltage vectors. However, this strategy requires the traversal optimization of 25 voltage vector combinations, which introduces a significant computational burden. To reduce the number of iterations, the authors of [18] propose an improved dual-vector method that optimizes the cost function twice. When selecting the second voltage vector, only the two active voltage vectors and zero vectors adjacent to the first voltage vector are considered, without considering the other four active voltage vectors, resulting in a certain loss of steady-state performance. The authors of [19] propose a dual-vector predictive torque control algorithm that eliminates the weight factors of torque and flux, and determines the candidate vector combination by calculating the angle of the reference voltage vector. The process of solving the angle of the reference voltage vector involves much computation, and it uses voltage instead of minimizing current tracking errors as the goal in the cost function, which requires additional voltage sampling circuits. If the reference voltage value from the previous cycle is used to approximate the sampling voltage, it will cause a certain degree of error.

To further improve the control performance of the algorithm, some scholars continue to increase the voltage vector that is acting during the sampling period. In 2018, scholars proposed two three-vector predictive current control algorithms [20,21]. The authors of [20] equivalently synthesized a virtual voltage vector using three primary voltage vectors in each sector, and used the six virtual voltage vectors synthesized from the six sectors as candidate voltage vectors. Then, the optimal voltage vector combination was selected through cost function optimization. The strategy proposed in [21] determines the combination of three vectors by performing two cost function optimizations. Firstly, the voltage vector that minimizes the cost function is selected as the first among the six active voltage vectors. Then, the first voltage vector is combined with the other five active voltage vectors, zero vectors are inserted to synthesize five candidate virtual voltage vectors in total, and another round of cost function optimization is performed to find the virtual voltage vector that minimizes the cost function and acts on the inverter driving motor. Although the literature [20,21] covers the generated voltage vector up to any amplitude and in any direction, further improving the steady-state performance of the system, the computational complexity is relatively large. The authors of [22] propose a method of selecting the optimal vector combination by calculating the angle of the reference voltage vector, and designing a cost function to solve the action time of the selected optimal vector combination. However, the calculation process of the reference voltage vector is still complex, and the derivation

operation is involved in calculating the action time of the vector. The algorithm still has some space to reduce computational complexity. The authors of [23] propose a scheme that combines three vectors and extended voltage vectors, aiming to expand the vectors' coverage range. However, the final validation results show that its improvement effect is limited. The authors of [24] propose a predictive torque control scheme based on a switch table, which achieves fast voltage vector selection and reduces computational complexity. However, due to the omission of cost function evaluation, the accuracy of the selection of the optimal vector combination cannot be fully guaranteed.

The above three-vector predictive control methods have greatly improved the steady-state performance of the system, but due to the increasing number of application vectors, the complexity and computational complexity of the algorithm have also increased accordingly. To ensure the implementation of other algorithm functions in the system, how to reduce the high computational burden of three vector control while ensuring a certain steady-state performance of the system has become a vital engineering application problem and research focus [25,26].

According to the above analysis, predictive control for both the speed and current of a motor drive system can solve the influence of the PI controller bandwidth and saturation effect, and improve the system's dynamic response performance, while MPC itself has no complex parameter tuning process. Based on this idea, the authors of [27] proposed a single-loop predictive control scheme for electric motors, which achieves the control of speed and current in one loop without a cascaded mechanism. Although the overall structure of the system is simplified, the cost function of single loop control is too complex, including the design of many weight coefficients, and the predictive equation becomes more cumbersome, increasing the computational burden. In addition, the adaptability and stability of parameters under different operating conditions cannot be fully guaranteed. For this reason, a cascaded predictive control method is proposed in [28,29], which retains the cascaded structure of the speed loop and current loop, and improves the overall control performance of the system. However, the current inner loop adopts the deadbeat predictive current control algorithm, increasing the computational complexity of the inner loop algorithm. Moreover, the authors of [29] use a fuzzy algorithm in the speed loop to determine the control weights of the PI controller and the predictive speed controller, limiting the complete performance of the predictive speed controller and increasing the computational burden.

Because the industrial servo field of CNC machine tools require the rapid realization of different cutting speeds, precision part machining, especially, also needs to take into account the smooth feeding of the tool and the workpiece, so for the motor to provide power, it is necessary to take into account the good performance of various aspects. This type of occasion on the one hand requires a rapid dynamic response, while ensuring good steady-state performance, on the other hand, also requires a low cost of hardware. This article proposes an improved cascaded predictive control method applied to PMSM. Firstly, the nominal predictive speed controller is designed based on the idea of a generalized predictive control algorithm. Secondly, an extended state observer (ESO) is designed to observe the system disturbance and compensate for the nominal predictive speed controller. The two constitute the predictive speed controller of the outer speed loop. A low-complexity three-vector predictive current control algorithm is proposed for the current inner loop of a cascaded structure. Firstly, two sets of candidate voltage vector combinations are determined by judging the imaginary polarity of the current error vector when the zero vector acts alone. Then, two traversal calculations are performed to obtain the optimal voltage vector acting on the three-phase two-level inverter to drive the PMSM. The low-complexity cascaded model predictive control proposed in this article simultaneously combines good dynamic performance with a low algorithm calculation time, and effectively reduces the required hardware cost; at the same time, its steady-state performance is comparable to that of the FOC method which has superior steady-state performance, and is better-adapted to speedy working conditions.

2. Mathematical Model of PMSM

Assuming that the magnetic circuit is not saturated and the magnetic field is sinusoidal, ignoring hysteresis and eddy current losses, the mathematical model of PMSM in a rotating coordinate system can be established as

$$\begin{bmatrix} u_d \\ u_q \end{bmatrix} = R_s \begin{bmatrix} i_d \\ i_q \end{bmatrix} + \frac{d}{dt} \begin{bmatrix} \psi_d \\ \psi_q \end{bmatrix} + p\omega_m \begin{bmatrix} 0 & -1 \\ 1 & 0 \end{bmatrix} \begin{bmatrix} \psi_d \\ \psi_q \end{bmatrix} \tag{1}$$

where for the d-axis and q-axis, the stator voltages are u_d and u_q, respectively, the stator currents are i_d and i_q, the stator flux linkages are ψ_d and ψ_q, ω_m is the rotor mechanical angular velocity, and p is the number of pole pairs.

The stator flux linkage equation of PMSM can be expressed as

$$\begin{bmatrix} \psi_d \\ \psi_q \end{bmatrix} = \begin{bmatrix} L_d & 0 \\ 0 & L_q \end{bmatrix} \begin{bmatrix} i_d \\ i_q \end{bmatrix} + \begin{bmatrix} \psi_f \\ 0 \end{bmatrix} \tag{2}$$

where $L_d = L_q = L_s$ is the stator winding inductance for a surface-mounted permanent magnet synchronous motor, and ψ_f is the rotor flux linkage.

Then, the electromagnetic torque equation and mechanical equation of PMSM can be expressed, respectively, as

$$T_e = \frac{3}{2} p[(L_d - L_q) i_d i_q + \psi_f i_q] \tag{3}$$

$$d\omega_m/dt = (T_e - T_L - B\omega_m)/J \tag{4}$$

where J is the moment of inertia, T_e is the electromagnetic torque, T_L is the load torque, and B is the friction coefficient.

3. Principle of the Proposed Cascaded Model Predictive Control Method

The system structure of the cascaded predictive control method proposed in this article for PMSM is shown in Figure 1. The system uses the cascaded structure of speed outer and current inner loops. Both the speed loop and current loop use predictive control algorithms. The speed outer loop introduces an extended state disturbance observer based on the nominal predictive speed controller, and the current inner loop uses a three-vector low-complexity predictive control algorithm. The following is the specific design process.

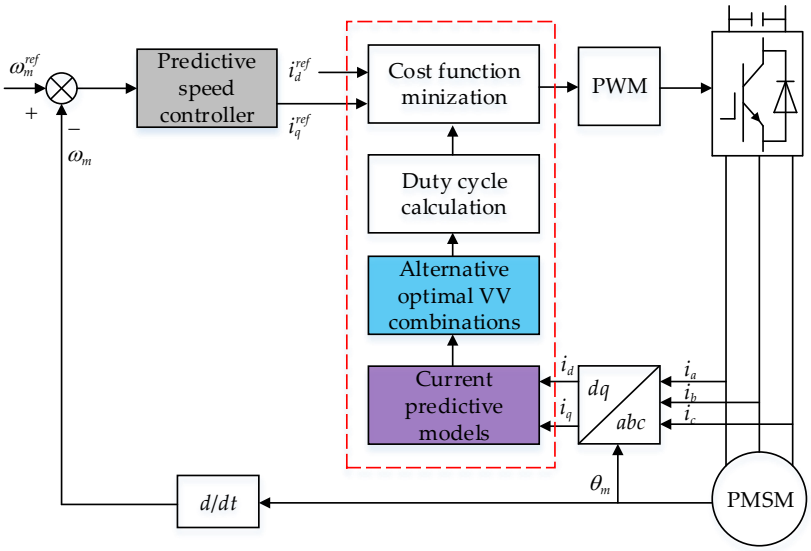

Figure 1. Structure of PMSM cascaded predictive control system.

3.1. Model Predictive Speed Control Algorithm

First, define $x = \omega_m$ as the state variable; the input variable is i_q, the output variable is $y = \omega_m$, and the disturbance variable is zero. Then, the system state equation can be given as

$$\begin{cases} dx/dt = d\omega_m/dt = -B\omega_m/J + 3p[(L_d - L_q)i_d + \psi_f]i_q/(2J) \\ y = \omega_m \end{cases} \tag{5}$$

Simplify its representation to obtain the following

$$\begin{cases} dx/dt = f(x) + g_1(x)u \\ y = h(x) = g_2(x)x \end{cases} \tag{6}$$

where $f(x) = -B\omega_m/J$, $g_1(x) = 3p[(L_d - L_q)i_d + \psi_f]/(2J)$, and $g_2(x) = 1$, $u = i_q$.

Second, the cost function including the reference speed and predicted speed is defined as follows:

$$F_{sp} = \frac{1}{2}\int_0^{T_{sp}} \left[\omega_m^{pre}(t+\tau) - \omega_m^{ref}(t+\tau)\right]^2 d\tau \tag{7}$$

where T_{sp} is the predicted time domain, $\omega_m^{pre}(t+\tau)$ is the predicted speed, and $\omega_m^{ref}(t+\tau)$ is the reference speed at $t+\tau$.

The relative order of the system is $\rho = 1$, and the system's control order is set to $r = 0$; then, the zero-order derivative and first-order derivative of the predicted speed can be given as

$$\omega_m^{pre}(t) = L_f^0 h(x) \tag{8}$$

$$d\omega_m^{pre}(t)/dt = L_f h(x) + L_{g_1} h(x)u(t) \tag{9}$$

Then, according to the Taylor series, $\omega_m^{pre}(t+\tau)$ and $\omega_m^{ref}(t+\tau)$ can expand at time t as follows:

$$\begin{cases} \omega_m^{pre}(t+\tau) = \Gamma(\tau)\overline{W}_{pre}(t) \\ \omega_m^{ref}(t+\tau) = \Gamma(\tau)\overline{W}_{ref}(t) \end{cases} \tag{10}$$

where $\Gamma(\tau) = \begin{bmatrix} 1 & \tau \end{bmatrix}$, $\overline{W}_{pre}(t) = \begin{bmatrix} \omega_m^{pre}(t) & d\omega_m^{pre}(t)/t \end{bmatrix}^{\mathrm{T}}$, and $\overline{W}_{ref}(t) = \begin{bmatrix} \omega_m^{ref}(t) & d\omega_m^{ref}(t)/dt \end{bmatrix}^{\mathrm{T}}$.

According to $\overline{\Gamma}(T_{sp}) = \int_0^{T_{sp}} \Gamma^{\mathrm{T}}(\tau)\Gamma(\tau)d\tau$,

$$\overline{\Gamma}(T_{sp})_{(i,j)} = T_{sp}^{i+j-1}/[(i-1)!(j-1)!(i+j-1)] \quad i,j = 1,2,\ldots,\rho+1. \tag{11}$$

Finally, according to Equation (11), Equation (7) can be expressed as

$$F_{sp} = \frac{1}{2}\left[\overline{W}_{pre}(t) - \overline{W}_{ref}(t)\right]^{\mathrm{T}}\overline{\Gamma}(T_{sp})\left[\overline{W}_{pre}(t) - \overline{W}_{ref}(t)\right] \tag{12}$$

When the cost function is the smallest, the reference speed is tracked, that is, $\partial F_{sp}/\partial u = 0$, and the speed-predicted control law can be obtained as follows:

$$u(t) = -\left\{(2J/3p)/[(L_d - L_q)i_d + \psi_f]\right\}[3(\omega_m - \omega_m^{ref})/(2T_{sp}) - B\omega_m/J - d\omega_m^{ref}/dt] \tag{13}$$

The speed-predicted controller's output is the q-axis current's reference value.

The above speed-predictive controller is designed based on the nominal model of the system, without considering the impact of load torque and parameter changes. Therefore, the speed will have the steady-state error when the load torque is large or the parameter changes significantly. Hence, the following design the extended state observer to observe

the disturbance and feedforward compensation to the q-axis current loop, improving the robustness of the predictive speed controller.

The basic idea of ESO is to estimate unknown disturbances through measurable quantities. The specific design process is as follows:

According to Equations (3) and (4),

$$d\omega_m/dt = (K_T/J)i_q - (T_L + T_f)/J \tag{14}$$

where $K_T = (3p/2)[(L_d - L_q)i_d + \psi_f]$, and $T_f = B\omega_m$.

Considering the change in motor parameters and load disturbances, Equation (14) is separated according to the standard weight and disturbance:

$$d\omega_m/dt = (K_{TN}/J_N)i_q + \Delta(K_{TN}/J_N)i_q - (T_L + T_f)/J \tag{15}$$

If $r(t)$ represents the total disturbance variable, which can be obtained via

$$r(t) = \Delta(K_{TN}/J_N)i_q - (T_L + T_f)/J \tag{16}$$

Equation (15) can be expressed as

$$d\omega_m/dt = (K_{TN}/J_N)i_q + r(t) \tag{17}$$

Let $r(t)$ be the extended state quantity; there is the extended state equation

$$\begin{cases} d\hat{\omega}_m/dt = (K_{TN}/J_N)i_q + r(t) + k_1(\omega_m - \hat{\omega}_m) \\ d\hat{r}(t)/dt = k_2(\omega_m - \hat{\omega}_m) \end{cases} \tag{18}$$

If $L = \begin{bmatrix} \hat{\omega}_m & \hat{r}(t) \end{bmatrix}^{\mathrm{T}}$, and $y = \omega_m$,

$$\begin{cases} dL/dt = AL + \begin{bmatrix} K_{TN}/J_N & 0 \end{bmatrix}^{\mathrm{T}} i_q + \begin{bmatrix} k_1 & k_2 \end{bmatrix}^{\mathrm{T}} (y - \hat{y}) \\ \hat{y} = CL \end{cases} \tag{19}$$

where $A = \begin{bmatrix} 0 & 1 \\ 0 & 0 \end{bmatrix}$, $C = \begin{bmatrix} 1 & 0 \end{bmatrix}$.

According to the pole assignment method, λ can be regarded as the ideal characteristic polynomial

$$\lambda = \left| sI - (A - \begin{bmatrix} k_1 & k_2 \end{bmatrix}^{\mathrm{T}} C) \right| = s^2 + k_1 s + k_2 = (s + k)^2 \tag{20}$$

From Equation (20), $k_1 = 2k$, and $k_2 = k^2$ can be taken, where $-k(k > 0)$ is the closed-loop expected pole of ESO. Finally, the structure block diagram of the predictive speed control algorithm with ESO designed is shown in Figure 2.

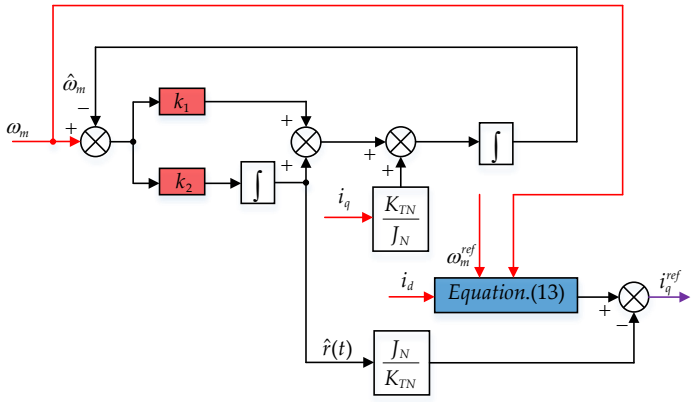

Figure 2. The structure block diagram of the model predictive speed controller.

3.2. Model Predictive Current Control Algorithm

1. Predictive Current Model

For a surface-mounted permanent magnet synchronous motor, the stator current of the dq-axes in the two-phase rotating coordinate system is as follows:

$$\frac{d}{dt}\begin{bmatrix} i_d \\ i_q \end{bmatrix} = \frac{1}{L_s}\left\{ \begin{bmatrix} u_d \\ u_q \end{bmatrix} - R_s \begin{bmatrix} i_d \\ i_q \end{bmatrix} - p\omega_m \begin{bmatrix} 0 & -L_s \\ L_s & 0 \end{bmatrix} \begin{bmatrix} i_d \\ i_q \end{bmatrix} - p\omega_m \begin{bmatrix} 0 \\ \psi_f \end{bmatrix} \right\} \tag{21}$$

Using the first-order Euler formula to discretize Equation (21), the prediction model of the stator current of the dq-axes is

$$\begin{bmatrix} i_d(k+1) \\ i_q(k+1) \end{bmatrix} = \begin{bmatrix} i_d(k) \\ i_q(k) \end{bmatrix} + \frac{T_s}{L_s}\left\{ \begin{bmatrix} u_d(k) \\ u_q(k) \end{bmatrix} - R_s \begin{bmatrix} i_d(k) \\ i_q(k) \end{bmatrix} - p\omega_m \begin{bmatrix} 0 & -L_s \\ L_s & 0 \end{bmatrix} \begin{bmatrix} i_d(k) \\ i_q(k) \end{bmatrix} - p\omega_m \begin{bmatrix} 0 \\ \psi_f \end{bmatrix} \right\} \tag{22}$$

2. Analysis and Calculation of Current Error Vector

According to the current, predicted via Equation (22), of the surface-mounted permanent magnet synchronous motor, when the zero vector acts alone, the predicted value of the stator current of the *dq*-axes in the next control cycle is

$$\begin{bmatrix} i_{0d}(k+1) \\ i_{0q}(k+1) \end{bmatrix} = \begin{bmatrix} i_d(k) \\ i_q(k) \end{bmatrix} + \frac{T_s}{L_s}\left\{ -R_s \begin{bmatrix} i_d(k) \\ i_q(k) \end{bmatrix} - p\omega_m \begin{bmatrix} 0 & -L_s \\ L_s & 0 \end{bmatrix} \begin{bmatrix} i_d(k) \\ i_q(k) \end{bmatrix} - p\omega_m \begin{bmatrix} 0 \\ \psi_f \end{bmatrix} \right\} \tag{23}$$

Correspondingly, according to Equation (23), Equation (22) for the surface-mounted permanent magnet synchronous motor can be expressed as follows

$$\begin{bmatrix} i_d(k+1) \\ i_q(k+1) \end{bmatrix} = \begin{bmatrix} i_{0d}(k+1) \\ i_{0q}(k+1) \end{bmatrix} + \frac{T_s}{L_s}\begin{bmatrix} u_d(k) \\ u_q(k) \end{bmatrix} \tag{24}$$

Then, based on the predicted current when the reference value of the *dq*-axes current acts alone with the zero vector, the prediction error of the zero vector acting alone can be obtained as follows:

$$\begin{bmatrix} \delta_{0d}(k+1) \\ \delta_{0q}(k+1) \end{bmatrix} = \begin{bmatrix} i_d^{ref} - i_{0d}(k+1) \\ i_q^{ref} - i_{0q}(k+1) \end{bmatrix} \tag{25}$$

When the active voltage vector is applied, based on the reference value of the *d*-axis current and the predicted current of the active voltage vector, the current prediction error under the action of the active voltage vector can be obtained as follows

$$\begin{bmatrix} \delta_d(k+1) \\ \delta_q(k+1) \end{bmatrix} = \begin{bmatrix} i_d^{ref} - i_d(k+1) \\ i_q^{ref} - i_q(k+1) \end{bmatrix} \tag{26}$$

Furthermore, according to Equations (24) and (25), Equation (26) can be equivalently represented as

$$\begin{bmatrix} \delta_d(k+1) \\ \delta_q(k+1) \end{bmatrix} = \begin{bmatrix} i_d^{ref} - i_{0d}(k+1) - T_s u_d(k)/L_s \\ i_q^{ref} - i_{0q}(k+1) - T_s u_q(k)/L_s \end{bmatrix} = \begin{bmatrix} \delta_{0d}(k+1) - T_s u_d(k)/L_s \\ \delta_{0q}(k+1) - T_s u_q(k)/L_s \end{bmatrix} \tag{27}$$

Based on the above analysis, the effect of zero and active voltage vectors on stator current is shown in Figure 3. From Equation (27) and Figure 3, it can be observed that the partial effect of the active voltage vector on the stator current within a control cycle is equivalent to the full effect of the single action of the zero vector.

Due to the various possible voltage vector combinations in traditional three-vector model predictive current control methods, the following details a simplified selection scheme for the optimal vector combination based on the current prediction error to reduce redundant voltage vector combinations.

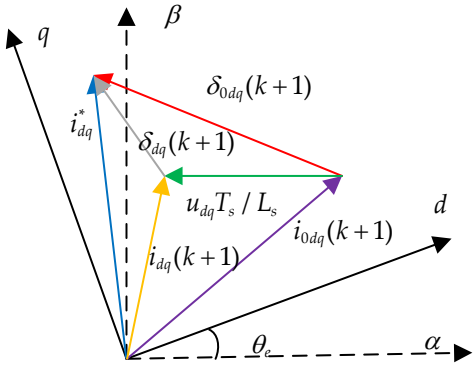

Figure 3. The effect of zero and active voltage vectors on stator current.

According to Equation (27), the optimal dq-axes' voltage components of the voltage vector that can be used to compensate for current prediction errors are obtained via

$$\begin{bmatrix} u_d^{opt}(k+1) \\ u_q^{opt}(k+1) \end{bmatrix} = \frac{L_s}{T_s} \begin{bmatrix} \delta_{0d}(k+1) \\ \delta_{0q}(k+1) \end{bmatrix} \tag{28}$$

Figure 3 shows that the optimal voltage vector can be directly determined using the current prediction error when the zero vector acts alone.

3. Determination of Candidate Voltage Vector Combinations

In addition, the entire complex plane can be divided into two half-planes according to the imaginary axis's positive and negative polarity, as shown in Figure 4. The current prediction error is based on the zero vector's action in complex plane β. The polarity of the axis component can determine the half-plane of the optimal voltage vector, thus eliminating redundant voltage vectors. Compared with traditional three-vector model predictive current control, the proposed optimal vector combination selection method based on the current prediction error vector can effectively reduce the number of listed voltage vectors, avoid traversing all possible voltage vector combinations, and reduce complexity.

$$\begin{bmatrix} \delta_{0\alpha}(k+1) \\ \delta_{0\beta}(k+1) \end{bmatrix} = \begin{bmatrix} \cos\theta_e & -\sin\theta_e \\ \sin\theta_e & \cos\theta_e \end{bmatrix} \begin{bmatrix} \delta_{0d}(k+1) \\ \delta_{0q}(k+1) \end{bmatrix} \tag{29}$$

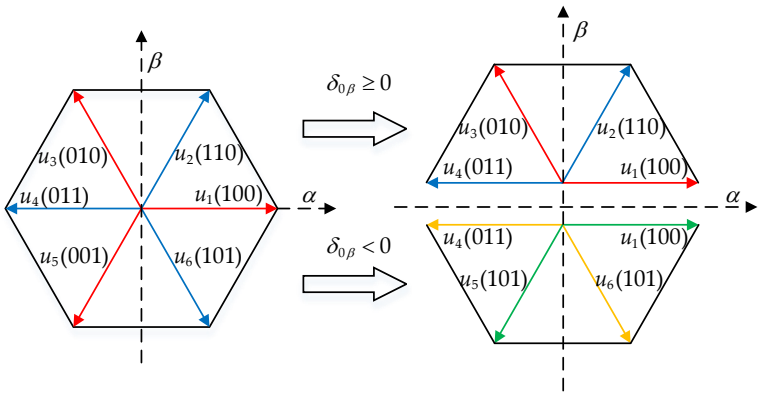

Figure 4. Schematic diagram for selecting the optimal voltage vector combination.

After transforming the current error vector generated by the zero vector acting along from a rotating coordinate system to a stationary coordinate system, the candidate voltage vector combination is determined by the following principles.

Condition 1: If $\delta_{0\beta} \geq 0$, indicating that the optimal voltage vector is located at $[0, \pi]$, $(u_1, u_3, u_{0,7})$ or $(u_2, u_4, u_{0,7})$ should be selected to synthesize the optimal voltage vector combination.

Condition 2: If $\delta_{0\beta} < 0$, indicating that the optimal voltage vector is located at $(\pi, 2\pi)$, $(u_4, u_6, u_{0,7})$ or $(u_5, u_1, u_{0,7})$ should be selected to synthesize the optimal voltage vector combination.

4. Duty Cycle Calculation and Cost Function Minimization

In terms of calculating the duty cycle of two active and zero-voltage vectors in the selected optimal voltage vector combination, when the zero vector acts alone, the two active voltage vectors selected based on the polar selection of the imaginary part of the current prediction error vector are marked as u_i and u_j, respectively.

After determining the three primary voltage vectors, virtual voltage vectors can be synthesized by allocating the action time of the voltage vectors. This article adopts the principle of deadbeat in the *dq*-axes' current to calculate the vector action time, so that the predicted value of the *dq*-axes' current is equal to the given value.

$$\begin{bmatrix} i_d(k+1) \\ i_q(k+1) \end{bmatrix} = \begin{bmatrix} i_d(k) \\ i_q(k) \end{bmatrix} + t_i \begin{bmatrix} s_{id} \\ s_{iq} \end{bmatrix} + t_j \begin{bmatrix} s_{jd} \\ s_{jq} \end{bmatrix} + t_{0,7} \begin{bmatrix} s_{0d} \\ s_{0q} \end{bmatrix} = \begin{bmatrix} i_d^{ref} \\ i_q^{ref} \end{bmatrix} \tag{30}$$

According to Equation (22), the calculation formula for the slope of the *dq*-axes' current under the action of the zero-voltage vector is

$$\begin{bmatrix} s_{0d} \\ s_{0q} \end{bmatrix} = \frac{1}{L_s} \left\{ -R_s \begin{bmatrix} i_d(k) \\ i_q(k) \end{bmatrix} - p\omega_m \begin{bmatrix} 0 & -L_s \\ L_s & 0 \end{bmatrix} \begin{bmatrix} i_d(k) \\ i_q(k) \end{bmatrix} - p\omega_m \begin{bmatrix} 0 \\ \psi_f \end{bmatrix} \right\} \tag{31}$$

The slope of the *dq*-axes' current when the two active voltage vectors in the candidate vector combination act is shown in Equations (32) and (33)

$$\begin{bmatrix} s_{id} \\ s_{iq} \end{bmatrix} = \begin{bmatrix} s_{0d} \\ s_{oq} \end{bmatrix} + \frac{1}{L_s} \begin{bmatrix} u_{id} \\ u_{iq} \end{bmatrix} \tag{32}$$

$$\begin{bmatrix} s_{jd} \\ s_{jq} \end{bmatrix} = \begin{bmatrix} s_{0d} \\ s_{0q} \end{bmatrix} + \frac{1}{L_s} \begin{bmatrix} u_{jd} \\ u_{jq} \end{bmatrix} \tag{33}$$

The sum of the action times of the two active voltage vectors and the zero vector is the sampling period. That is, by combining Equations (30)–(33), the action times of the three voltage vectors can be obtained as follows:

$$t_i = \frac{T_s(s_{0q}s_{jd} - s_{jq}s_{0d}) + [i_d^{ref} - i_d(k)](s_{jq} - s_{0q}) + [i_q^{ref} - i_q(k)](s_{0d} - s_{jd})}{s_{0q}(s_{jd} - s_{id}) + s_{iq}(s_{0d} - s_{jd}) + s_{jq}(s_{id} - s_{0d})} \tag{34}$$

$$t_j = \frac{T_s(s_{iq}s_{0d} - s_{0q}s_{id}) + [i_d^{ref} - i_d(k)](s_{0q} - s_{iq}) + [i_q^{ref} - i_q(k)](s_{id} - s_{0d})}{s_{0q}(s_{jd} - s_{id}) + s_{iq}(s_{0d} - s_{jd}) + s_{jq}(s_{id} - s_{0d})} \tag{35}$$

$$t_{0,7} = T_s - t_i - t_j \tag{36}$$

The ratio of the action time of each of the three voltage vectors to the sampling period is their respective duty cycle, and the components of the corresponding synthesized virtual voltage vector on the *dq*-axes are

$$\begin{bmatrix} u_d \\ u_q \end{bmatrix} = \begin{bmatrix} u_{id} & u_{jd} \\ u_{iq} & u_{jq} \end{bmatrix} \begin{bmatrix} t_i/T_s \\ t_j/T_s \end{bmatrix} \tag{37}$$

According to Equation (37), we can calculate the virtual voltage vector corresponding to the DC and AC axis components synthesized by combining two sets of AC voltage vectors, and then substitute it into the predicted current model Equation (22) to obtain the predicted current value. Then, the virtual voltage vector that minimizes the cost function

is selected as the optimal output of the inverter to achieve motor drive control. The cost function used in this article is shown in Equation (38):

$$F_{cu} = |\Delta i_d| + |\Delta i_q| \tag{38}$$

where we can minimize current tracking errors with $|\Delta i_d| = \left|i_d^{ref} - i_d(k+1)\right|$, and $|\Delta i_q| = \left|i_q^{ref} - i_q(k+1)\right|$.

As mentioned earlier, when the current error vector's imaginary axis component is greater than or equal to zero, there are two combinations of $(u_1, u_3, u_{0,7})$ and $(u_2, u_4, u_{0,7})$; at this time, there are three possible regions where the reference voltage vector is located, which are Sector I, Sector II, and Sector III, respectively. When the current error vector's imaginary axis component is less than zero, there are two combinations of $(u_4, u_6, u_{0,7})$ and $(u_5, u_1, u_{0,7})$. At this time, the reference voltage vector also has three possible regions, sector IV, sector V, and sector VI, as shown in Figure 5.

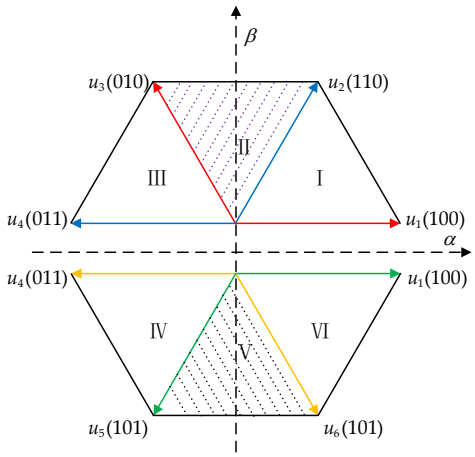

Figure 5. Sector distribution in the complex plane where the space voltage vector is located.

The optimization process can be further concluded as follows. First, we should analyze the case of the upper half of a complex plane.

(1) If the cost function obtained by combining voltage vectors $(u_1, u_3, u_{0,7})$ is smaller than that obtained via $(u_2, u_4, u_{0,7})$, then $(u_1, u_3, u_{0,7})$ is selected to further generate the inverter drive signal through a seven-segment pulse width modulation method;

(2) If the cost function obtained by combining voltage vectors $(u_2, u_4, u_{0,7})$ is less than or equal to the cost function obtained via $(u_1, u_3, u_{0,7})$, then we can select $(u_2, u_4, u_{0,7})$ to further generate the inverter drive signal through a seven-segment pulse width modulation method;

Next, we should analyze the case of the lower half of the complex plane.

(3) If the cost function obtained by combining voltage vectors $(u_4, u_6, u_{0,7})$ is smaller than that obtained via $(u_5, u_1, u_{0,7})$, then $(u_4, u_6, u_{0,7})$ is selected to further generate the inverter drive signal through a seven-segment pulse width modulation method;

(4) If the cost function obtained by combining voltage vectors $(u_5, u_1, u_{0,7})$ is less than or equal to the cost function obtained via $(u_4, u_6, u_{0,7})$, then $(u_5, u_1, u_{0,7})$ is selected to further generate the inverter drive signal through a seven-segment pulse width modulation method;

In addition, it should be noted that the optimal voltage vector combination obtained through cost function comparison and optimization requires the duty cycle of each voltage vector within the combination calculated above, and a further combination with the seven-segment pulse width modulation method to naturally determine the final driving pulse signal acting on the inverter. This is also its unique advantage; that is, through the idea of duty cycle, the modulation effect that originally requires six voltage vector combinations is achieved by combining four sets of voltage across the entire complex plane. This pulse modulation idea can be better understood by referring to [30].

Finally, in order to present more clearly the four alternative voltage vector combinations combined with seven-segment pulse width modulation that ultimately affect the drive pulse signal of the inverter, Figures A12–A15 in Appendix A of the article provides a detailed presentation. It can be found that compared to traditional methods such as SVPWM, they do not bring more switching jumps.

To more clearly demonstrate the lower computational complexity of the proposed cascaded model predictive control method, Method 4, compared to that of the traditional method, Method 3, the algorithm flowcharts of Method 3 and Method 4 in the control inner loop are provided, as shown in Figures 6 and 7, respectively. It can be observed that the proposed improvement in Method 4 reduces the combination of candidate voltage vectors from six to two groups with minimal computational complexity by flexibly using the current error vector when the zero vector acts alone. This only requires two sets of duty cycle calculations and two sets of cost functions to be calculated and traversed for optimization in each sampling period, while the traditional method, Method 3, requires six sets of duty cycle calculations and six sets of cost functions to be calculated and traversed for optimization. From a qualitative perspective, the superiority of the proposed method, Method 4, is demonstrated. In Section 5, the two algorithms will be verified through experiments to further verify the effectiveness of the proposed method, Method 4, in reducing the calculation burden of the algorithm.

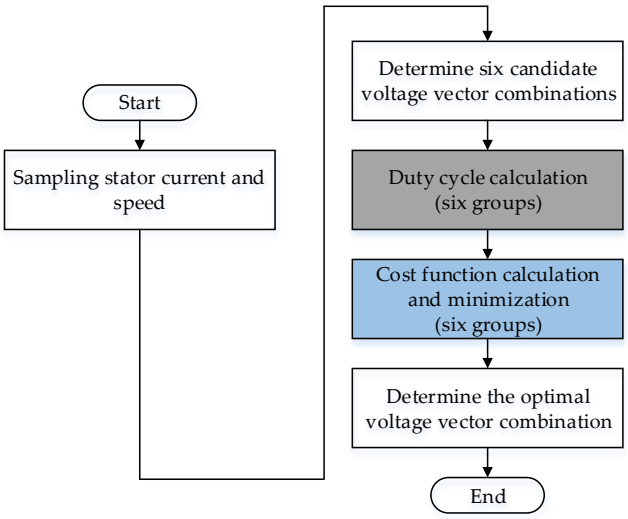

Figure 6. Cascaded model predictive control inner loop flowchart for Method 3.

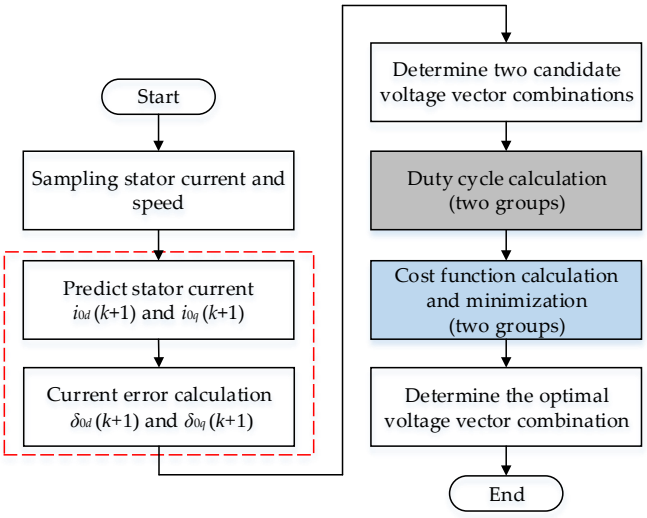

Figure 7. Cascaded model predictive control inner loop flowchart for Method 4.

4. Simulation Verification

The improved cascade predictive control algorithm proposed in this article will be simulated, validated, and compared with traditional algorithms. The surface-mounted PMSM parameters used in the simulation are shown in Table 1.

Table 1. PMSM parameters for the simulation.

Parameters	Symbol	Value
Rated torque	T_N	5 N · m
Rated speed	ω_m	1000 rpm
Stator inductance	L_s	8.2 mH
Stator phase resistance	R_s	0.9585 Ω
Number of pole pairs	p	4
Flux linkage of permanent magnets	ψ_f	0.1827 Wb
DC-bus voltage	U_{dc}	300 V
Rotational inertia	J	0.006329 kg · m^2

The rated speed is set as the reference speed of the motor, we start with no load, and then suddenly apply the rated load in 0.5 s. The methods compared are as follows. Method 1 is the traditional double loop PI control method, Method 2 is the speed loop predictive control and current loop PI control method, Method 3 is the cascaded predictive control method based on the current inner loop using the traditional three vectors, and Method 4 is the proposed cascade predictive control method based on the current inner loop using the improved three vectors. The simulation comparison results of the four methods are shown in Figure 8.

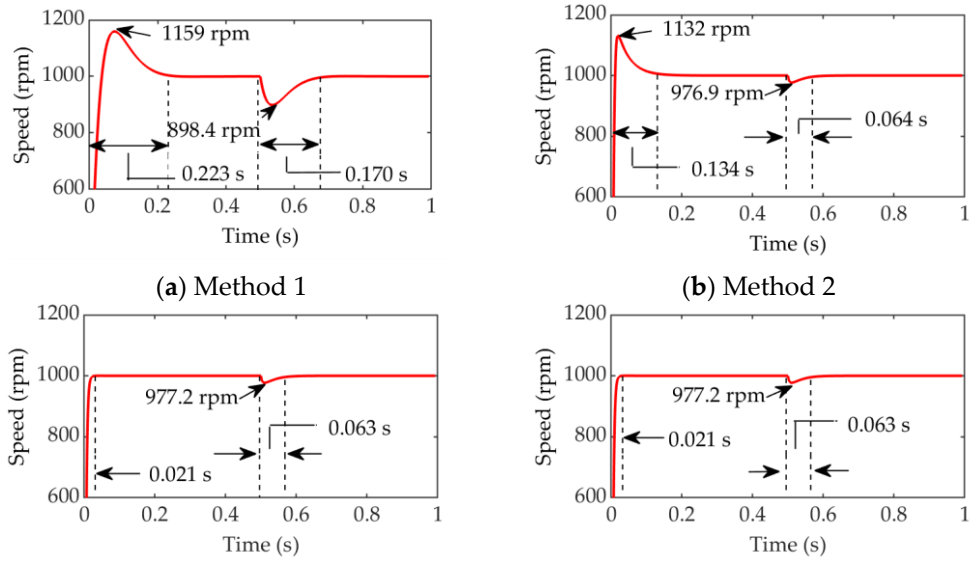

(**a**) Method 1 (**b**) Method 2

(**c**) Method 3 (**d**) Method 4

Figure 8. Speed response curves of four methods.

From Figure 8, it can be found that with Method 1, when both the speed outer loop and the current inner loop use PI controllers, the dynamic performance and anti-interference ability of the permanent magnet synchronous motor are poor; when Method 2 is adopted, that is, the predictive speed control algorithm based on ESO is adopted in the speed outer loop, the dynamic performance and anti-interference ability of the PMSM are improved; when using Method 3 and Method 4, which replace the PI controller of the current inner loop with a predictive current control algorithm based on three vectors based on Method 2, the dynamic performance and anti-interference ability of the PMSM are significantly improved.

Furthermore, the quantitative results of the speed dynamic performance of Methods 1–4 are shown in Table 2.

Table 2. Quantitative analysis of the dynamic performance of four control methods.

Method (1~4)	Starting Overshoot	Response Time	Speed Drop after Loading	Speed Recovery Time after Loading
Method 1	15.9%	0.223 s	101.6 rpm	0.170 s
Method 2	13.2%	0.134 s	23.1 rpm	0.064 s
Method 3	0	0.021 s	22.8 rpm	0.063 s
Method 4	0	0.021 s	22.8 rpm	0.063 s

From Table 2, it can be found that in terms of overshoot, Method 2 decreased by 2.7% compared to Method 1, with a decrease rate of 17%. However, Method 3 and Method 4 do not have overshoots. In terms of response time, Method 2 decreased by 0.089 s compared to Method 1, with a reduction rate of 40%. However, the two cascaded predictive control methods, Method 3 and Method 4, reduced the response time by 0.202 s compared to Method 1 and 0.113 s compared to Method 2, with a response time of only 0.021 s. When the sudden load was applied, the speed drop of Method 2 decreased from the value of 101.6 rpm of Method 1 to 23.1 rpm, and the improvement rate of anti-interference performance was 77.3%. The anti-interference performance of Method 3 and Method 4 was similar to that of Method 2; at the same time, the speed recovery time of Methods 2–4 was reduced by about 62.4% compared to that of Method 1.

The above analysis of the speed performance indicators of PMSM shows that Method 3 and Method 4 have the best dynamic and anti-interference performance, and the improvement effect is significant.

From the observations in Figures 9 and 10, it is found that the *d*-axis' current ripple under methods 1–4 is almost the same and remains at a relatively low level; the *q*-axis' current ripple under Methods 1–3 is close, while Method 4 has a slight increase in the *q*-axis current ripple compared to that of Methods 1–3. The above results demonstrate that using predictive control algorithms in the speed outer loop and current inner loop can still ensure that the PMSM has excellent steady-state performance comparable to that of the FOC used in the traditional method, Method 1. The three-phase stator current waveform of the proposed Method 4 is shown in Figure 11, and it can be found that the three-phase stator current waveform is smooth, with better sine and symmetry.

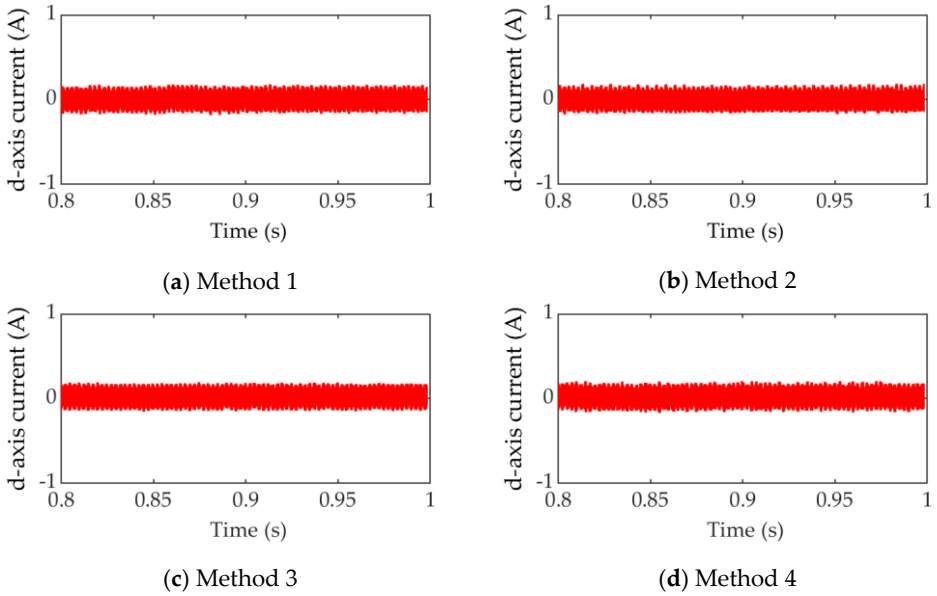

(**a**) Method 1 (**b**) Method 2

(**c**) Method 3 (**d**) Method 4

Figure 9. Steady-state *d*-axis current of four methods.

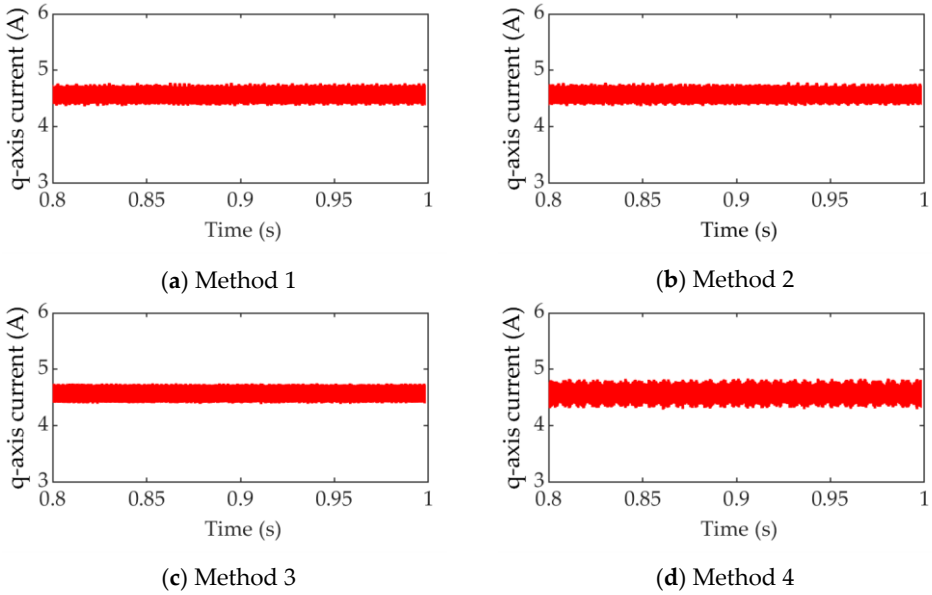

Figure 10. Steady-state q-axis current of four methods.

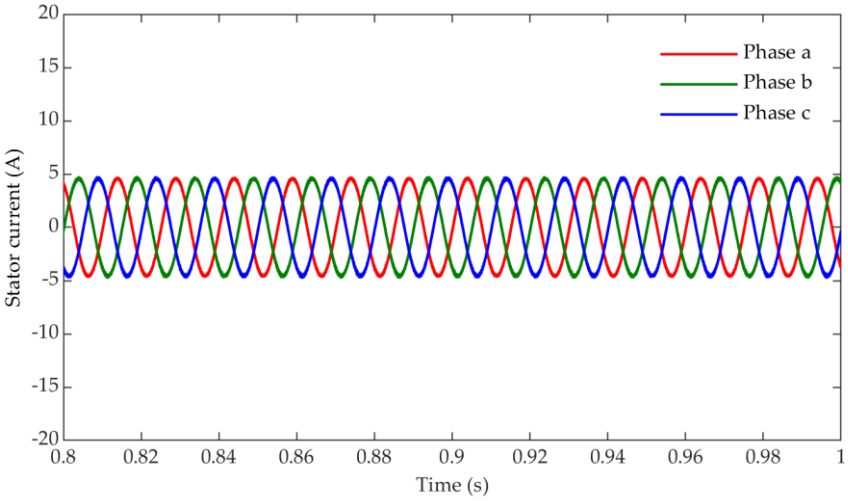

Figure 11. Three-phase stator current of proposed method, Method 4.

Further harmonic analysis was conducted on the proposed Method 4, with the PMSM operating at rated speed and rated torque, tested for five cycles, as shown in Figure 12.

Figure 12 shows that the THD content of the stator current in the proposed Method 4 is 2.15%, and the harmonic content is relatively low. In addition, the stator current harmonic results of methods 1–4 are shown in Table 3. The THD content of Method 3 is 2.05%, and the THD content of Methods 1–2 is 2.12%. The THD levels of the stator current of the four methods are all within the range of [2%, 3%], indicating that the proposed Method 4 has steady-state performance comparable to traditional Method 1 of FOC.

Table 3. Current THD data for four control methods.

Method (1~4)	Method 1	Method 2	Method 3	Method 4
THD of phase-a	2.12%	2.12%	2.05%	2.15%

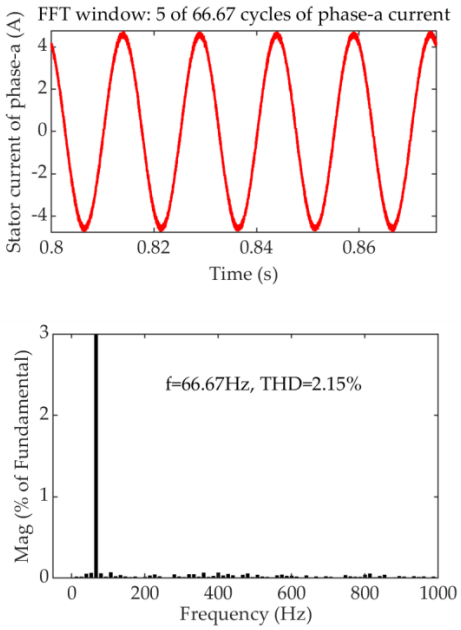

Figure 12. Current THD analysis of the proposed Method 4.

5. Experimental Test

To further validate the effectiveness of the proposed method, a fast control prototype motor experimental platform with dSPACE 1202 as the controller is constructed as shown in Figure 13. The sampling frequency is 10 kHz and the specific parameters of experimental motor are shown in Table 4.

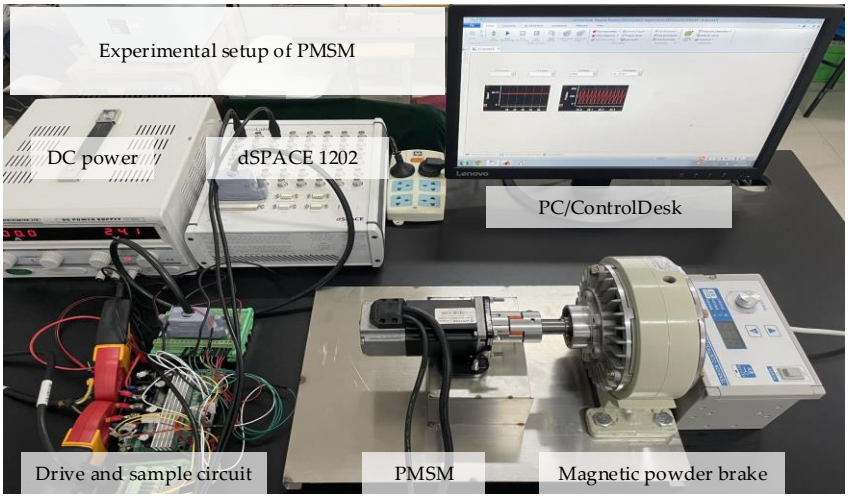

Figure 13. PMSM experimental setup.

Figure 14 is a schematic diagram of the structure of a surface-mounted permanent magnet synchronous motor test platform based on dSPACE. The test platform mainly includes surface mounted permanent magnet synchronous motor, dSPACE hardware platform, inverter circuit, DC power supply, and PC upper computer. The algorithm validation model is built using Matlab/Simulink, and then the parts connected to the motor and inverter circuit in the Simulink model are replaced with modules from the RTI library, The real-time connection between the Simulink control algorithm part and the central circuit part was achieved, and then the C code was automatically generated using RTW and downloaded to the dSPACE hardware platform. Then, the ControlDesk 6.0 upper computer software was started, and the suffix name. sdf object file was loaded. The motor

control parameters could be adjusted in real-time by entering the control system interface. At the end of the experiment, the speed record data was exported, visualized, and analyzed through Matlab.

Table 4. PMSM parameters for experiment.

Parameters	Symbol	Value
Rated torque	T_N	0.64 N · m
Rated speed	ω_m	3000 rpm
Stator inductance	L_s	0.8 mH
Stator phase resistance	R_s	0.4 Ω
Number of pole pairs	p	4
Flux linkage of permanent magnets	ψ_f	0.0147 Wb
DC-bus voltage	U_{dc}	24 V
Rotational inertia	J	0.000019 kg · m^2

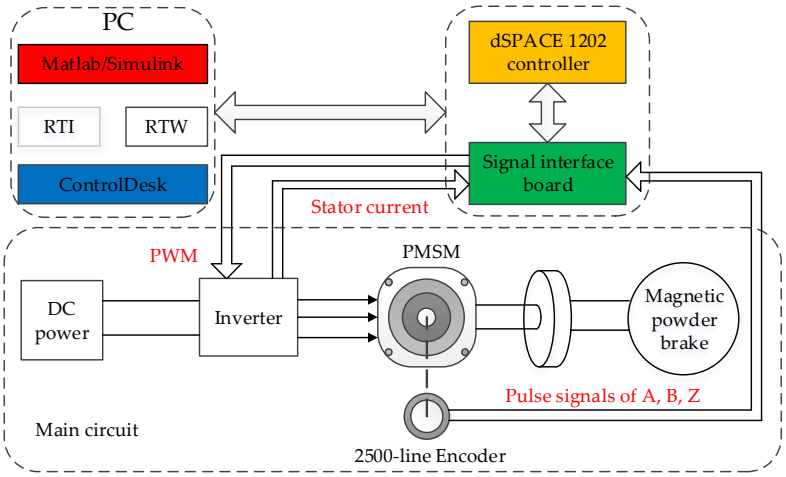

Figure 14. Schematic diagram of PMSM experimental setup principle.

Figures 15–17 show the steady-state experimental waveforms of the PMSM operating with four methods: 1800 rpm, 1500 rpm, and 1200 rpm.

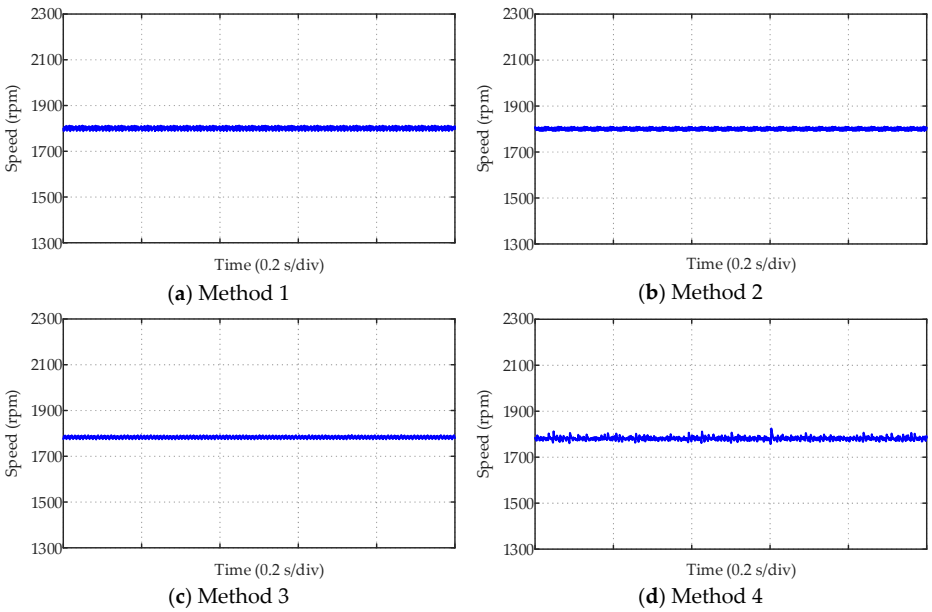

(**a**) Method 1 (**b**) Method 2

(**c**) Method 3 (**d**) Method 4

Figure 15. Steady-state speed experiment results of four methods running at 1800 rpm.

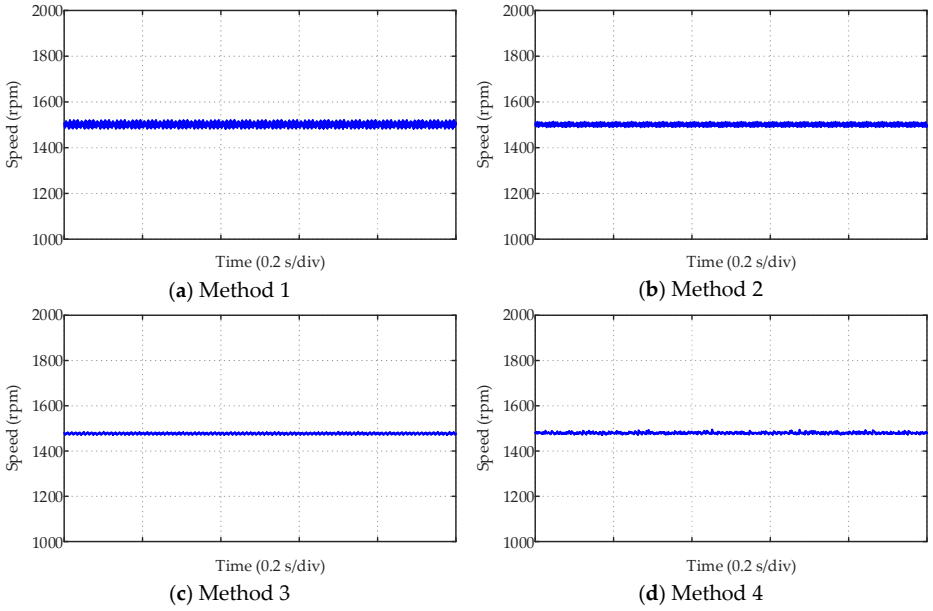

(**a**) Method 1 (**b**) Method 2

(**c**) Method 3 (**d**) Method 4

Figure 16. Steady-state speed experiment results of four methods running at 1500 rpm.

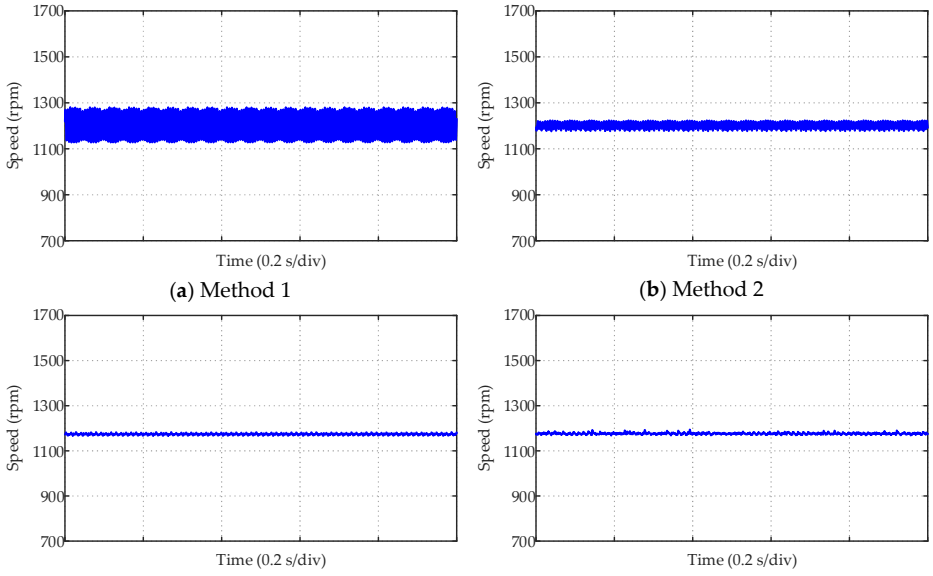

(**a**) Method 1 (**b**) Method 2

(**c**) Method 3 (**d**) Method 4

Figure 17. Steady-state speed experiment results of four methods running at 1200 rpm.

It can be seen that when the motor is operating at 1800 rpm, Method 3 based on the cascaded prediction algorithm has the most minor speed ripple. The speed ripple of the proposed cascaded prediction method, Method 4, based on the improved current inner loop three-vector prediction algorithm is similar to the speed ripple of Method 1 based on FOC, but is slightly larger than that of Method 3. As the rotational speed decreases, the steady-state performance of Method 1 and Method 2 continues to deteriorate, especially for Method 1 based on the FOC, which has a more severe degradation effect and exhibits significant speed ripples when operating at 1200 rpm.

However, both Method 3 and Method 4 based on the cascaded prediction algorithm maintained good steady-state performance, with a significantly lower speed ripple compared to that of Methods 1 and 2. This indicates that the proposed cascade prediction method has better adaptability and stability for switching speed conditions, and has better steady-state performance at low speeds.

To quantify the steady-state speed performance of the four methods under different speed conditions, this article evaluates the magnitude of the motor speed ripple by calculating the standard deviation of motor speed. The quantitative calculation results are shown in Table 5. In addition, in order to better reflect this trend of change, a line chart was further drawn for intuitive expression, as shown in Figure 18.

Table 5. Quantitative experimental data of the steady-state ripple of four methods at different speed conditions of the motor.

Method (1~4)	Method 1	Method 2	Method 3	Method 4
Ripple of 1800 rpm	6.160 rpm	4.846 rpm	4.558 rpm	7.117 rpm
Ripple of 1500 rpm	10.340 rpm	6.176 rpm	3.121 rpm	3.519 rpm
Ripple of 1200 rpm	49.579 rpm	13.938 rpm	3.719 rpm	3.567 rpm

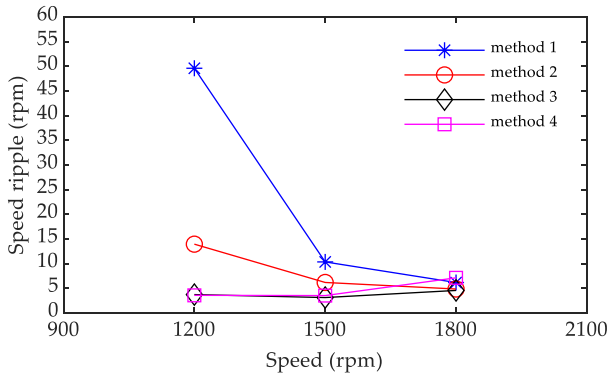

Figure 18. Experimental curves of the steady-state ripple of four methods under different speed conditions of the motor.

Then, the calculation burdens of Method 3 and Method 4 based on the cascaded prediction algorithm are compared. In the dSPACE1202 control system, turnaround time as a measurement of computational complexity can be read directly from the control desk, which includes the communication time between dSPACE and the control desk, the A/D conversion time, data-saving time, and code implementation time. Generally, the communication time, A/D conversion time, and data-saving time are basically the same for different control methods in the same experimental environments. Therefore, the main reason this article's two control methods have different turnaround times is that the code implementation time is different. From Table 6, it can be seen that the turnaround time of Method 3 is 19.96 µs, while that of Method 4 is about 13.48 µs.

Table 6. Turnaround time of the cascaded MPC methods, Method 3 and 4.

Method (3~4)	Method 3	Method 4
Turnaround time	19.96 µs	13.48 µs

Therefore, the experimental results indicate that compared with Method 3, the computational complexity of the proposed method is reduced dramatically.

To verify the dynamic performance of the proposed method in this article, Figure 19 presents experimental waveforms of the PMSM speed change under four different methods. The experimental results show that the response times of Method 3 and Method 4 based on the cascaded prediction algorithm are similar, significantly improving the response speed compared to that of Method 1 and Method 2. The speed switching response times of methods 1–4 are 29.91 ms, 33.77 ms, 10.58 ms, and 11.63 ms, respectively.

It is worth noting that in practical systems, due to the influence of hardware and digital control methods, there may be calculation delays, which means that the optimal

voltage vector does not immediately apply to the inverter drive motor at the beginning of each cycle. If the calculation delay is long, it will have an impact on the steady-state performance of the system. For this calculation of delay, the one-step delay compensation used in [31] is usually used.

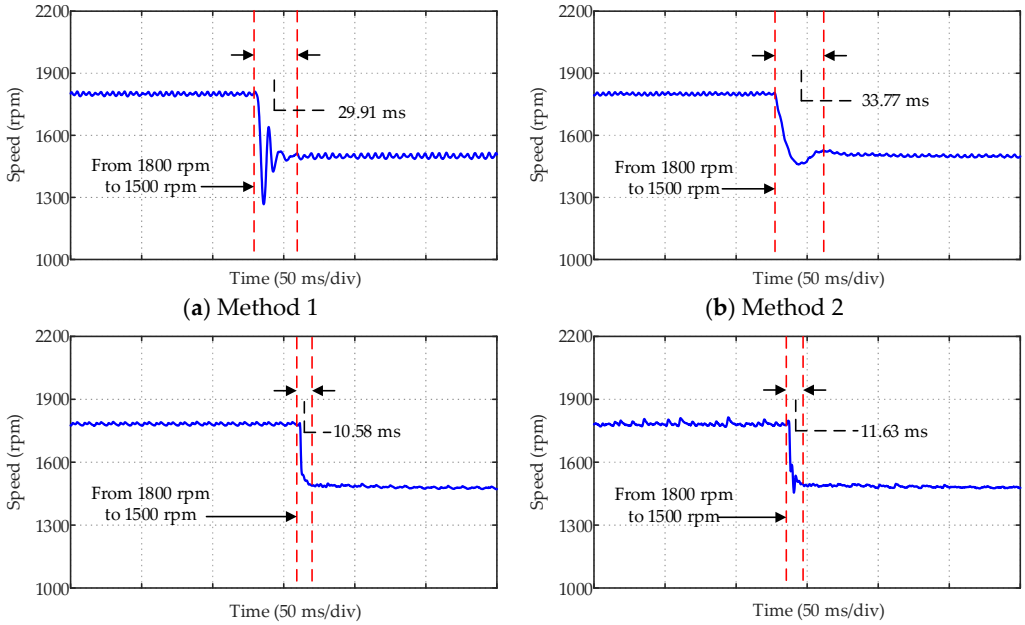

Figure 19. Speed response experimental results with Method 1–4.

Therefore, in this article, we conducted a mechanism analysis on the impact of calculation delay, as shown in Appendix A, Figures A1–A3. The focus was on analyzing the delay error caused by the system in two cases: a shorter calculation delay and longer calculation delay. Theory shows that the delay error is greater when the calculation delay is longer. Finally, the dynamic and steady-state performance of the system using the traditional one-step delay compensation strategy was verified through experiments, as shown in Figures A4 and A5 and Table A1 in Appendix A. The experimental results showed that the steady-state performance of the system decreased significantly when using the traditional one-step delay compensation strategy compared to that when not using this compensation strategy, and the dynamic performance slightly decreased, with little difference compared to when not using delay compensation.

According to the experimental results obtained in Appendix A, it can be seen that the algorithm execution time of the low-complexity cascaded model predictive control method proposed in this article is relatively short compared to the sampling period of 100 μs in actual systems. Therefore, when using a one-step delay compensation strategy, the delay error will be increased based on the aforementioned mechanism's analysis. Therefore, only when the sampling period and algorithm calculation delay are similar, using this one-beat delay compensation strategy has a better effect, and the experimental results are consistent with the conclusions described in [32].

In addition, in this article we also conducted an experimental analysis of the relationship between the steady-state performance and the sampling period of the proposed method, Method 4. Due to the need for the discretization of the mathematical model of the control object in model predictive control, the accuracy of model predictive control generally decreases sharply when the accuracy of the mathematical model or the discretization of the control object decreases. Usually, when the sampling frequency is much higher than the operating frequency of the motor, that is, when the frequency ratio is very high, the Euler discretization method can be used to establish a prediction model for permanent magnet synchronous motors. However, as the frequency ratio decreases, the error caused

by model discretization increases, leading to a significant decrease in prediction accuracy and steady-state performance, and even causing system instability.

In order to evaluate the impact of changes in the frequency ratio on the steady-state performance of the system, in this article we conducted an experimental verification and quantitative analysis of the steady-state speed performance of the motor under different frequency ratios. Finally, a line chart was drawn based on the calculated data to more intuitively and clearly reflect the impact of changes in the frequency ratio, as shown in Figures A6 and A7 in Appendix A.

The motor operates at 1500 rpm with a corresponding operating frequency of 100 Hz. The selected sampling frequencies are 10 kHz, 5 kHz, 4 kHz, 2.5 kHz, and 2 kHz, and the frequency ratios corresponding to each sampling frequency are 100, 50, 40, 25, and 20, respectively. Research has found that as the frequency ratio decreases, the speed ripple of the motor increases accordingly, especially in the range where the frequency ratio is less than 40; that is, when the sampling frequency is less than 4 kHz, the change in speed ripple is more rapid. When the frequency ratio is set to 20, the speed ripple reaches 102.477 rpm, and the steady-state control performance deteriorates seriously. This provides a reliable basis for selecting a reasonable sampling period and motor operating frequency.

Due to the need for the CNC machine tool to move the load workbench forward and backward, it is necessary for the motor to sometimes work in reverse mode. The mechanical structure diagram of the CNC machine tool is shown in Figure A8 of Appendix A. Therefore, in this article we describe conducting experimental comparisons of the four control methods under reverse operating conditions, in order to verify the effectiveness and practicality of the proposed method, Method 4, in more dimensions, as shown in Figures A9–A11 of Appendix A. The experimental results show that Method 1 based on FOC exhibits oscillation instability characteristics at the speeds of −1200 rpm, −1500 rpm, and −1800 rpm tested in the experiment. However, the performance of proposed method, Method 4, is very close to that of Method 3, which belongs to cascaded predictive control. Only Method 2, which uses predictive control in the speed loop, has poorer performance than methods 3 and 4 do. This indicates that Method 1 based on FOC has the optimal PI parameters under different operating conditions, and in general, it cannot achieve the real-time tuning of PI parameters, which makes its adaptability to operating conditions poor, especially in situations where operating conditions change frequently. The inner and outer control loops of the proposed method, Method 4, both use predictive algorithms, which make the adaptability of the working conditions better based on the predictive optimization control concept.

6. Conclusions

This article focuses on the application of CNC machine tools and selects a permanent magnet synchronous motor as the system servo motor. The main consideration is to use permanent magnet excitation instead of electric excitation, so that rotor winding has no induced current and the stator winding has a resistive load, resulting in high motor efficiency and a high power factor. At the same time, it eliminates the collector ring and brush, which improves reliability. In the research process of this article, a low-complexity cascaded model predictive control method was mainly proposed. The proposed method selects a composite scheme of a nominal predictive speed controller based on the generalized predictive algorithm and an extended state load disturbance observer in the control outer loop. In the control inner loop, the improvement of the three-vector predictive current algorithm with good steady-state performance but high computational complexity is mainly considered. By flexibly utilizing the current vector error under the action of the zero-voltage vector alone, the six sets of candidate voltage vectors in the traditional method are reduced to two sets for optimization selection. Finally, the dynamic and steady-state performances of the proposed method were verified through simulation and experimental platform comparison. Moreover, this article also extends the study of the impact of the ratio of sampling frequency to operating frequency on the steady-state performance of a motor, as well as the limitations of traditional one-step delay compensation strategies.

Through the analysis, simulation and experimental testing of the above mechanism, it can be concluded that the new cascade predictive control method proposed in this article has the following advantages:

(1) Compared to the traditional FOC-based method, Method 1, based on PI controllers, there is no need for complex control parameter tuning, and only adjusting the speed and current prediction cycle can change system performance;

(2) Both the simulation and experimental results show that compared with traditional FOC-based Method 1 or speed outer loop predictive control Method 2 that retains the current inner loop's PI controller, the proposed cascade predictive control methods, Method 3 and 4, have faster response speeds and significant improvement effects, with almost no loss of steady-state performance;

(3) For methods 3 and 4 which are based on cascaded predictive control, Method 4 significantly reduces computational complexity while ensuring minimal steady-state performance loss.

Moreover, considering that the steady-state performance of the motor will deteriorate as the ratio of the sampling frequency to the motor operating frequency decreases, the adaptability of the proposed low-complexity cascaded model predictive control method at low frequency ratios will be considered in the subsequent study; in addition, due to the calculation delay factor of the actual system, which also affects the steady-state performance of the system to a certain degree, the study of the delay compensation strategy will be considered in the subsequent study and adopted with greater accuracy. It should also be noted that when servo systems such as CNC machine tools use lower rigidity transmission devices, the motor and load can be considered as a two-mass system for modeling research. This article focuses on the general situation when the transmission device has higher rigidity. In addition, the use of more matching loading device will be considered in the subsequent research to complete the test of torque working conditions, which in turn will provide more technical support for the realization of industrialization.

Author Contributions: Q.M. performed the initial research that was the basis of the idea for this article. The conception of the comparison, the writing of the document, and verification were also predominantly performed by Q.M., the first author. G.B. has contributed in an advisory role, providing feedback and hints for presentation. All authors have read and agreed to the published version of the manuscript.

Funding: This research was funded by "National Natural Science Foundation of China, grant number No. 51967012" and "The Provincial Key R & D Program of Gansu, China, grant number No. 20YF8GA055".

Data Availability Statement: The data are not publicly available due to privacy.

Conflicts of Interest: The authors declare no conflict of interest.

Appendix A

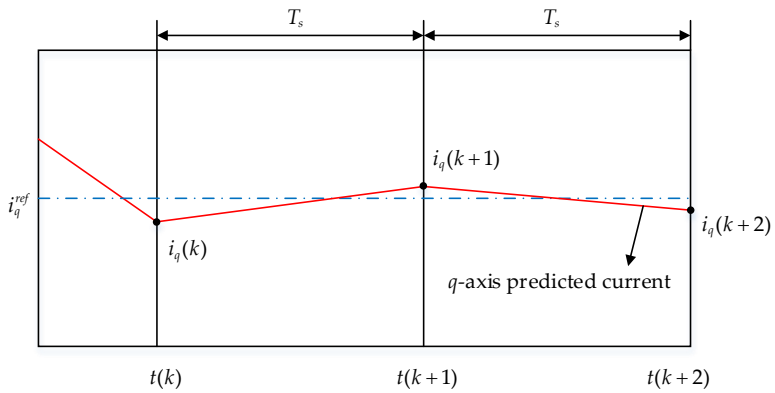

Figure A1. Model prediction method implementation without calculation delay in ideal cases.

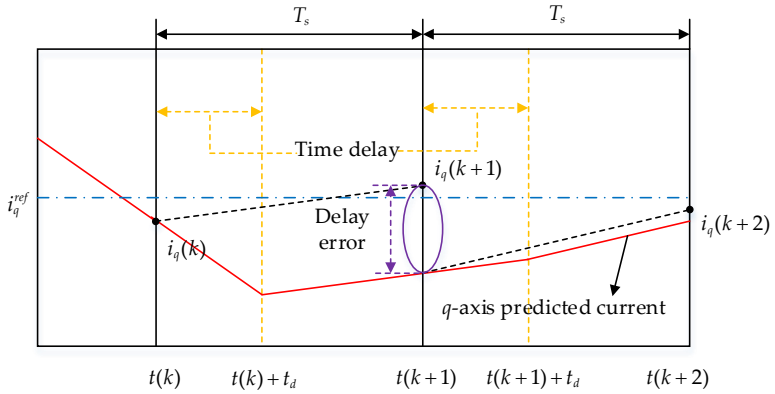

Figure A2. Model prediction method implementation with longer calculation delay in practical cases.

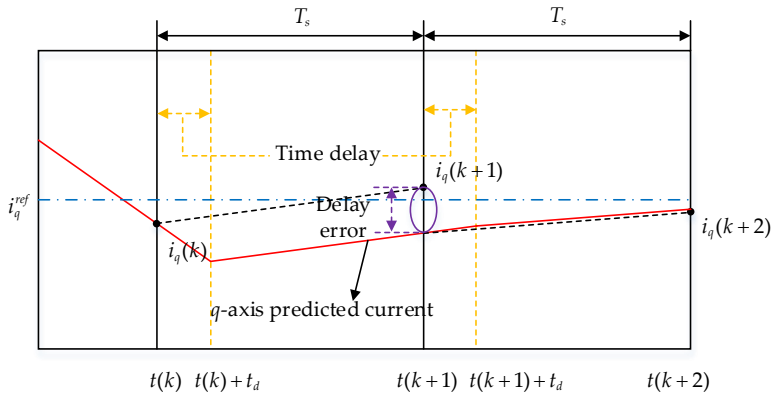

Figure A3. Model prediction method implementation with short calculation delay in practical cases.

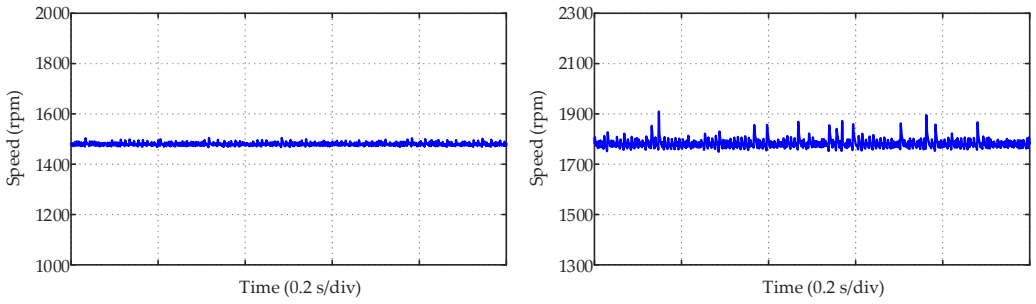

(**a**) 1500 rpm (**b**) 1800 rpm

Figure A4. Experimental results of steady-state speed of motor with one-step delay compensation using Method 4.

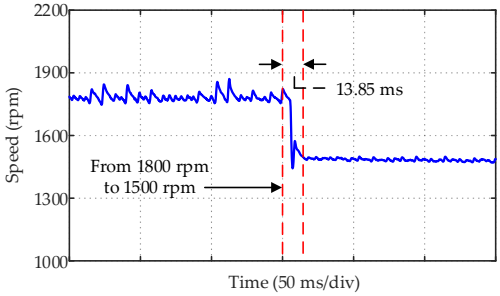

Figure A5. Experimental results of dynamic response of motor speed with one-step delay compensation using Method 4.

Table A1. Quantitative experimental data of steady-state speed ripple without delay compensation and with one-step delay compensation using Method 4.

Method 4	Without Delay Compensation	With Delay Compensation
Ripple of 1500 rpm	3.519 rpm	5.846 rpm
Ripple of 1800 rpm	7.117 rpm	16.540 rpm

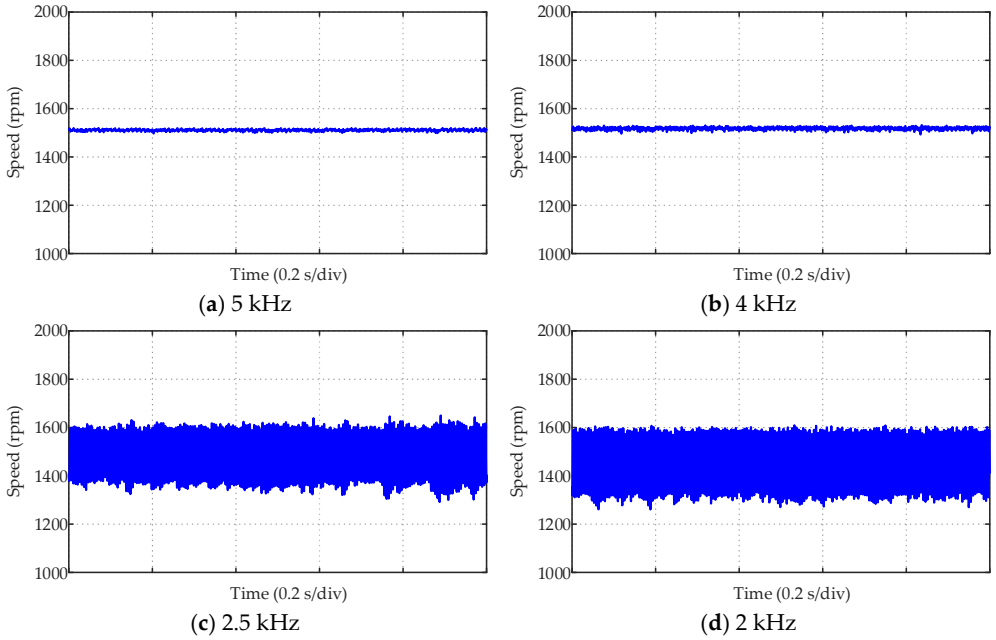

Figure A6. Method 4 Experimental results of motor running at 1500 rpm steady-state speed at different sampling frequencies.

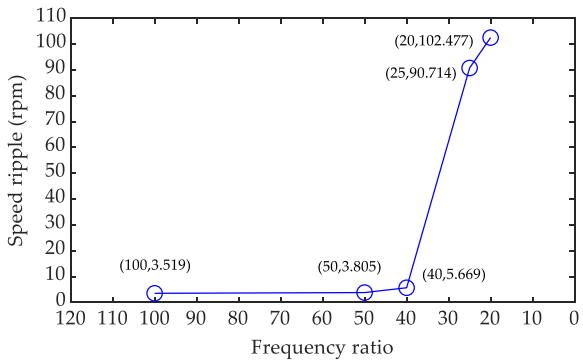

Figure A7. Experimental curves of a steady-state speed ripple of a motor running at 1500 rpm with a variation in the frequency ratio using Method 4.

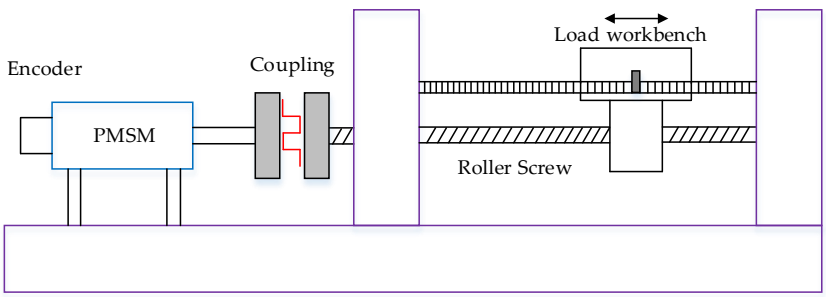

Figure A8. Mechanical structure diagram of CNC machine tools.

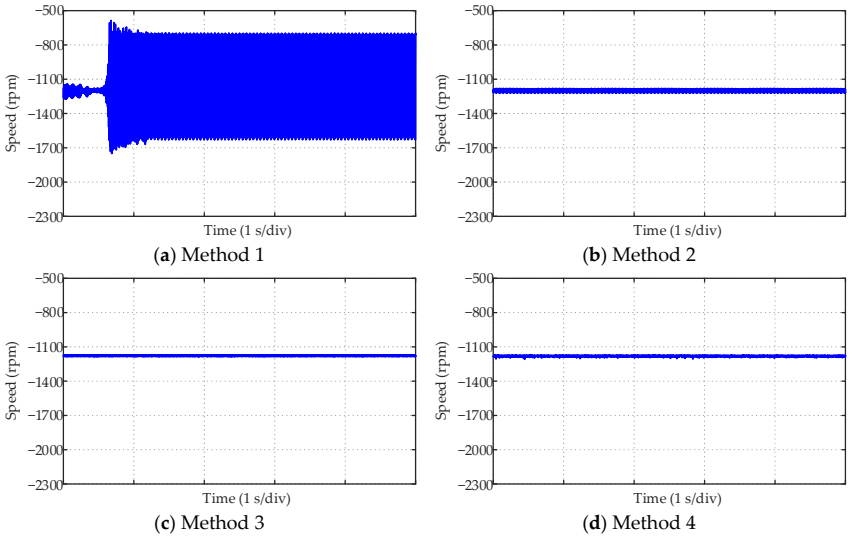

(**a**) Method 1 (**b**) Method 2

(**c**) Method 3 (**d**) Method 4

Figure A9. Steady-state speed experiment results of four methods running at −1200 rpm.

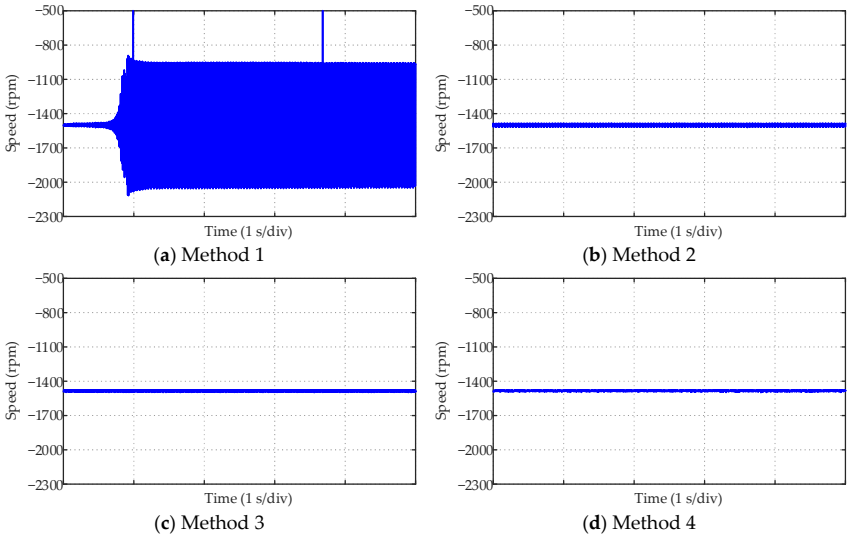

(**a**) Method 1 (**b**) Method 2

(**c**) Method 3 (**d**) Method 4

Figure A10. Steady-state speed experiment results of four methods running at −1500 rpm.

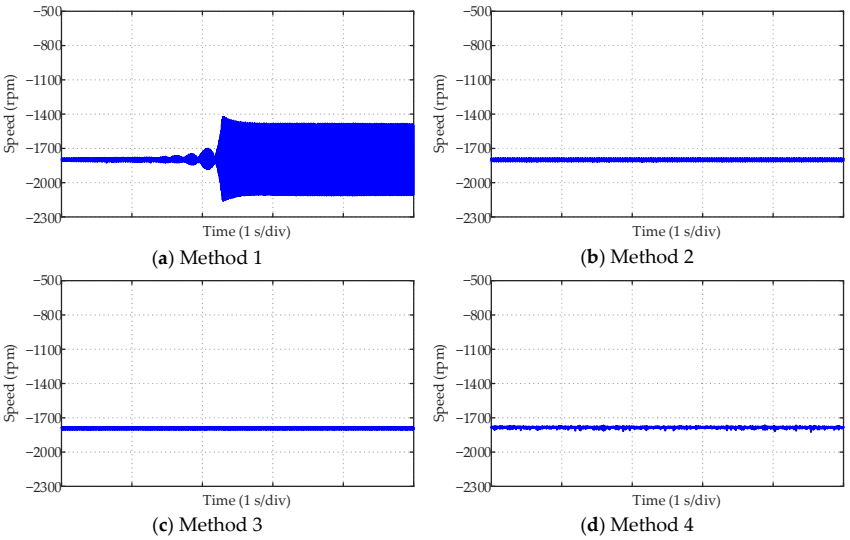

(**a**) Method 1 (**b**) Method 2

(**c**) Method 3 (**d**) Method 4

Figure A11. Steady-state speed experiment results of four methods running at −1800 rpm.

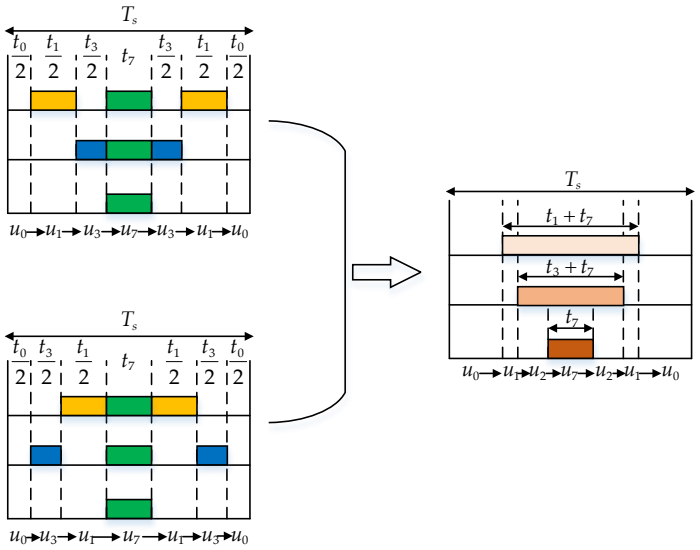

(**a**) The condition when $t_1 > t_3$

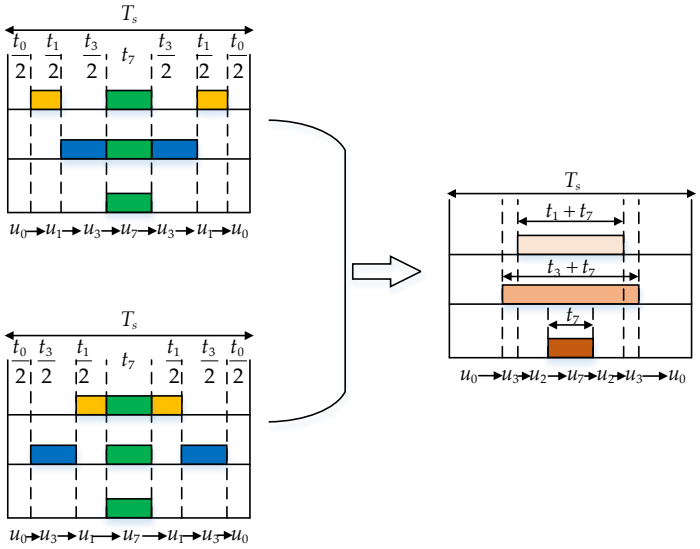

(**b**) The condition when $t_1 < t_3$

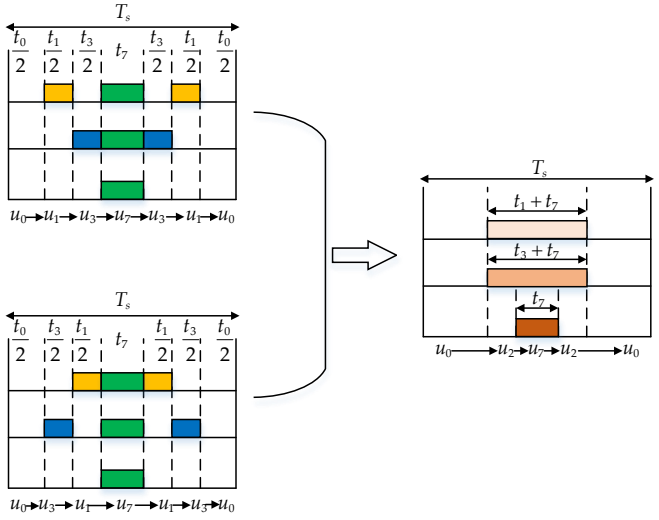

(**c**) The condition when $t_1 = t_3$

Figure A12. The condition when using the duty cycle obtained via (u_1, u_3, $u_{0,7}$) for modulation.

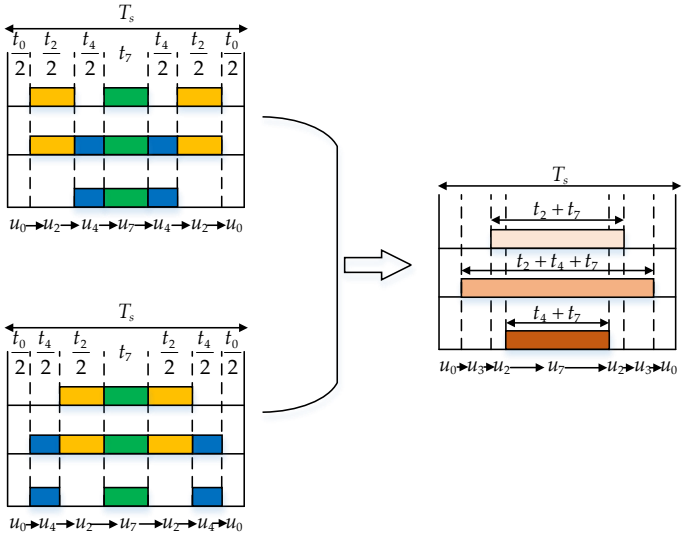

(**a**) The condition when $t_2 > t_4$

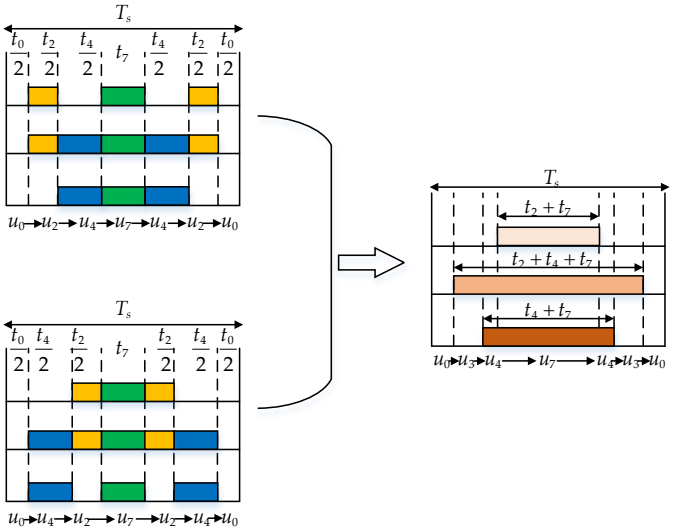

(**b**) The condition when $t_2 < t_4$

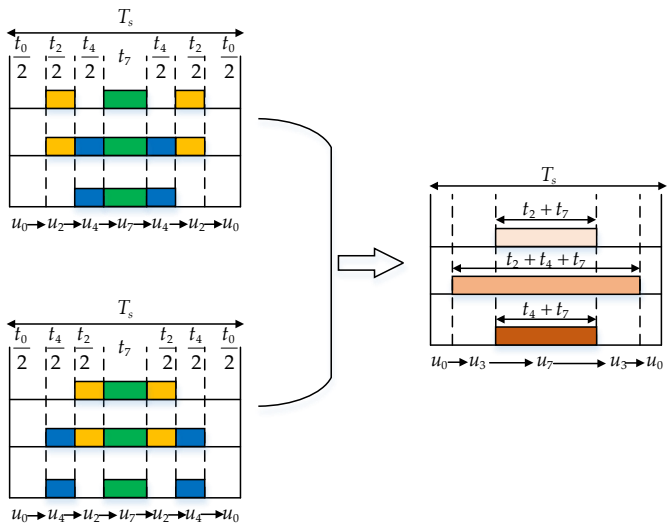

(**c**) The condition when $t_2 = t_4$

Figure A13. The condition when using the duty cycle obtained via (u_2, u_4, $u_{0,7}$) for modulation.

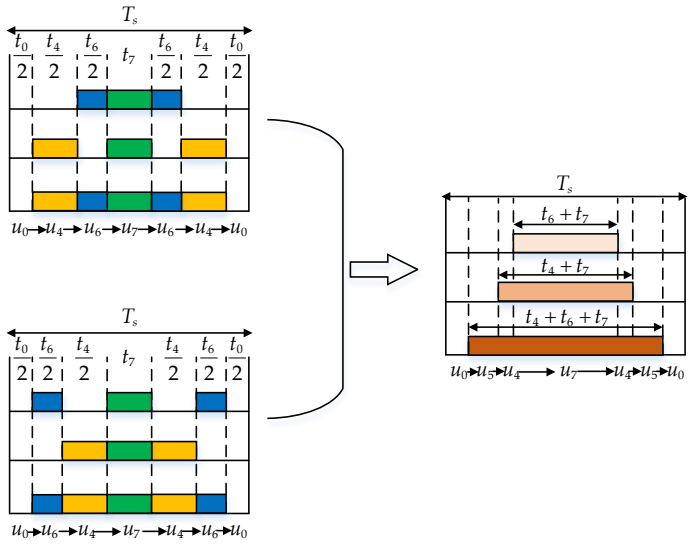

(**a**) The condition when $t_4 > t_6$

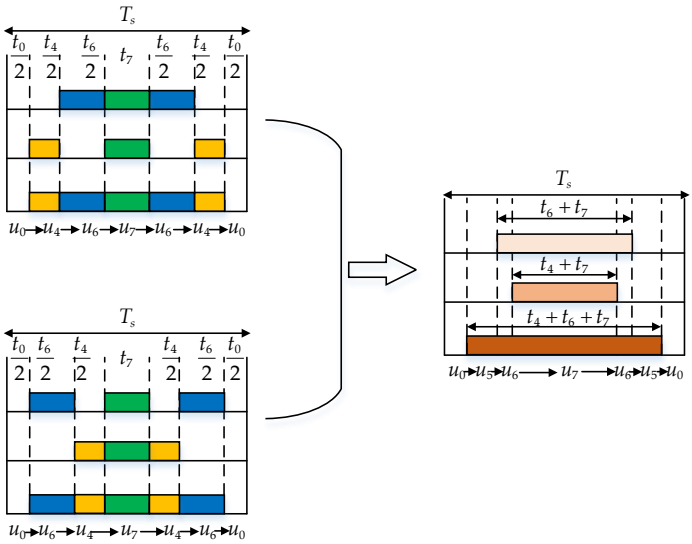

(**b**) The condition when $t_4 < t_6$

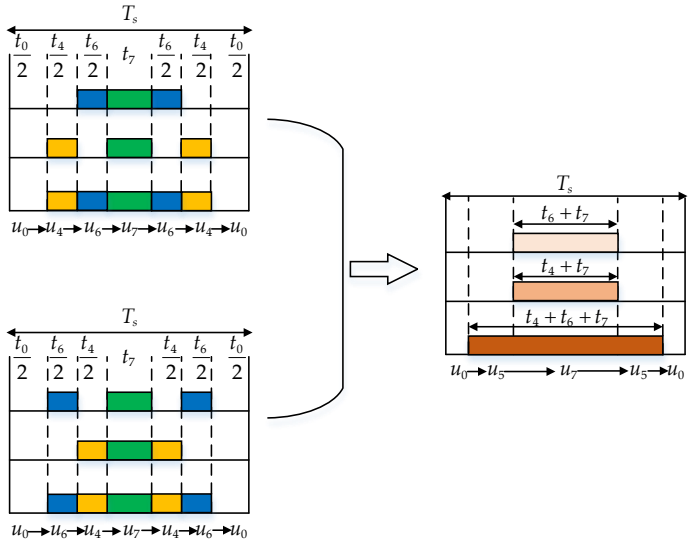

(**c**) The condition when $t_4 = t_6$

Figure A14. The condition when using the duty cycle obtained via (u_4, u_6, $u_{0,7}$) for modulation.

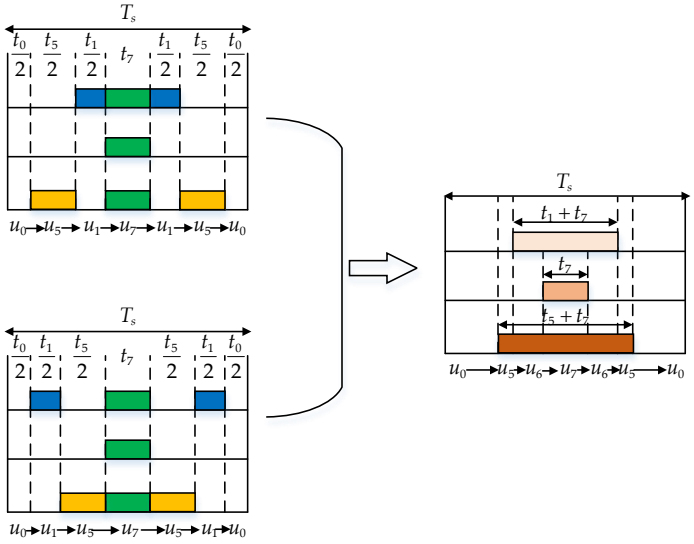

(**a**) The condition when $t_5 > t_1$

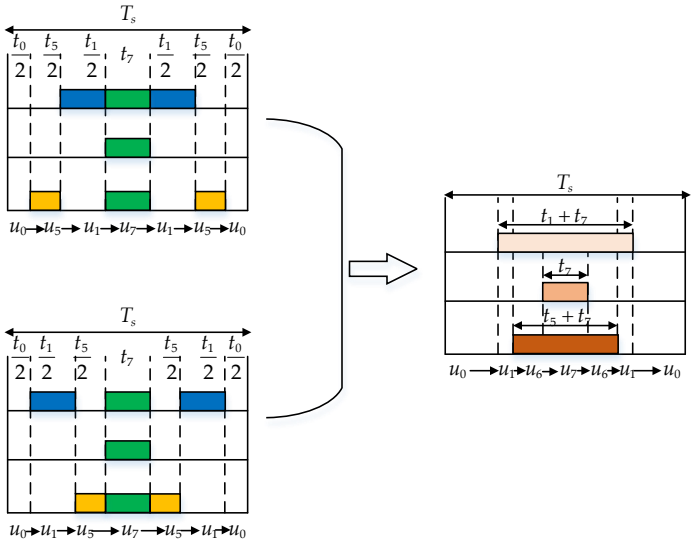

(**b**) The condition when $t_5 < t_1$

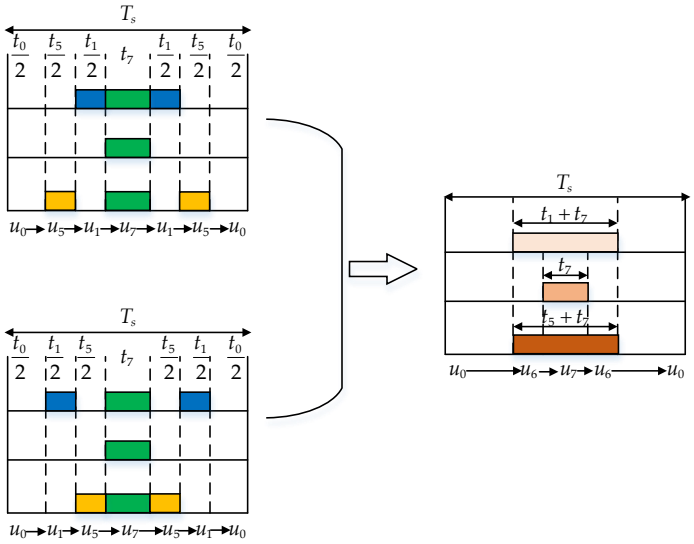

(**c**) The condition when $t_5 = t_1$

Figure A15. The condition when using the duty cycle obtained via (u_5, u_1, $u_{0,7}$) for modulation.

It should be noted that the above analysis is based on the situation where the duty cycle of both effective voltage vectors is not zero and the duty cycle of the effective voltage vector is zero, which can be simply derived and will not be listed here.

References

1. Sayed, E.; Abdalmagid, M.; Pietrini, G.; Sa'adeh, N.M.; Callegaro, A.D.; Goldstein, C.; Emadi, A. Review of Electric Machines in More-/Hybrid-/Turbo-Electric Aircraft. *IEEE Trans. Transport. Electrific.* **2021**, *7*, 2976–3005. [CrossRef]
2. Li, X.; Chau, K.T.; Cheng, M. Analysis, design and experimental verification of a field-modulated permanent-magnet machine for direct-drive wind turbines. *IET Electr. Power Appl.* **2015**, *9*, 150–159. [CrossRef]
3. Hong, D.K.; Hwang, W.; Lee, J.Y.; Woo, B.C. Design, Analysis, and Experimental Validation of a Permanent Magnet Synchronous Motor for Articulated Robot Applications. *IEEE Trans. Magn.* **2018**, *54*, 8207304. [CrossRef]
4. Choo, K.M.; Won, C.Y. Design and Analysis of Electrical Braking Torque Limit Trajectory for Regenerative Braking in Electric Vehicles with PMSM Drive Systems. *IEEE Trans. Power Electron.* **2020**, *35*, 13308–13321. [CrossRef]
5. Wu, G.; Huang, S.; Wu, Q.; Zhang, C.; Rong, F.; Hu, Y. Predictive Torque and Stator Flux Control for N∗3-Phase PMSM Drives with Parameter Robustness Improvement. *IEEE Trans. Power Electron.* **2021**, *36*, 1970–1983. [CrossRef]
6. Junejo, A.K.; Xu, W.; Mu, C.; Ismail, M.M.; Liu, Y. Adaptive Speed Control of PMSM Drive System Based a New Sliding-Mode Reaching Law. *IEEE Trans. Power Electron.* **2020**, *35*, 12110–12121. [CrossRef]
7. Chang, Y.C.; Chen, C.H.; Zhu, Z.C.; Huang, Y.W. Speed Control of the Surface-Mounted Permanent-Magnet Synchronous Motor Based on Takagi–Sugeno Fuzzy Models. *IEEE Trans. Power Electron.* **2016**, *31*, 6504–6510. [CrossRef]
8. Wang, Y.; Feng, Y.; Zhang, X.; Liang, J. A New Reaching Law for Antidisturbance Sliding-Mode Control of PMSM Speed Regulation System. *IEEE Trans. Power Electron.* **2020**, *35*, 4117–4126. [CrossRef]
9. Shao, M.; Deng, Y.; Li, H.; Liu, J.; Fei, Q. Robust Speed Control for Permanent Magnet Synchronous Motors Using a Generalized Predictive Controller with a High-Order Terminal Sliding-Mode Observer. *IEEE Access* **2019**, *7*, 121540–121551. [CrossRef]
10. Hu, M.; Hua, W.; Xiao, H.; Wang, Z.; Liu, K.; Cai, K.; Wang, Y. Fast Current Control without Computational Delay by Minimizing Update Latency. *IEEE Trans. Power Electron.* **2021**, *36*, 12207–12212. [CrossRef]
11. Devanshu, A.; Singh, M.; Kumar, N. An Improved Nonlinear Flux Observer Based Sensorless FOC IM Drive with Adaptive Predictive Current Control. *IEEE Trans. Power Electron.* **2020**, *35*, 652–666. [CrossRef]
12. Vafaie, M.H.; Dehkordi, B.M.; Moallem, P.; Kiyoumarsi, A. A New Predictive Direct Torque Control Method for Improving Both Steady-State and Transient-State Operations of the PMSM. *IEEE Trans. Power Electron.* **2016**, *31*, 3738–3753. [CrossRef]
13. An, X.; Liu, G.; Chen, Q.; Zhao, W.; Song, X. Robust Predictive Current Control for Fault-Tolerant Operation of Five-Phase PM Motors Based on Online Stator Inductance Identification. *IEEE Trans. Power Electron.* **2021**, *36*, 13162–13175. [CrossRef]
14. Niu, S.; Luo, Y.; Fu, W.; Zhang, X. Robust Model Predictive Control for a Three-Phase PMSM Motor with Improved Control Precision. *IEEE Trans. Ind. Electron.* **2021**, *68*, 838–849. [CrossRef]
15. Chen, W.; Zeng, S.; Zhang, G.; Shi, T.; Xia, C. A Modified Double Vectors Model Predictive Torque Control of Permanent Magnet Synchronous Motor. *IEEE Trans. Power Electron.* **2019**, *34*, 11419–11428. [CrossRef]
16. Morel, F.; Lin-Shi, X.; Rétif, J.M.; Allard, B.; Buttay, C. A Comparative Study of Predictive Current Control Schemes for a Permanent-Magnet Synchronous Machine Drive. *IEEE Trans. Ind. Electron.* **2009**, *56*, 2715–2728. [CrossRef]
17. Zhang, Y.; Yang, H. Generalized Two-Vector-Based Model-Predictive Torque Control of Induction Motor Drives. *IEEE Trans. Power Electron.* **2015**, *30*, 3818–3829. [CrossRef]
18. Zhang, Y.; Yang, H. Two-Vector-Based Model Predictive Torque Control Without Weighting Factors for Induction Motor Drives. *IEEE Trans. Power Electron.* **2016**, *31*, 1381–1390. [CrossRef]
19. Zhang, X.; Hou, B. Double Vectors Model Predictive Torque Control Without Weighting Factor Based on Voltage Tracking Error. *IEEE Trans. Power Electron.* **2018**, *33*, 2368–2380. [CrossRef]
20. Xu, Y.; Wang, J.; Zhang, B.; Zhou, Q. Three-Vector-Based Model Predictive Current Control for Permanent Magnet Synchronous Motor. *Trans. China Electrotech. Soc.* **2018**, *33*, 980–988.
21. Xu, Y.; Wang, J.; Zhou, Q.; Zhang, B. Double Optimization Three-vector-based Model Predictive Current Control for Permanent Magnet Synchronous Motors. *Proc. CSEE* **2018**, *38*, 1857–1864+1923.
22. Kang, S.W.; Soh, J.H.; Kim, R.Y. Symmetrical Three-Vector-Based Model Predictive Control with Deadbeat Solution for IPMSM in Rotating Reference Frame. *IEEE Trans. Ind. Electron.* **2020**, *67*, 159–168. [CrossRef]
23. Xu, B.; Jiang, Q.; Ji, W.; Ding, S. An Improved Three-Vector-Based Model Predictive Current Control Method for Surface-Mounted PMSM Drives. *IEEE Trans. Transport. Electrific.* **2022**, *8*, 4418–4430. [CrossRef]
24. Li, X.; Xue, Z.; Zhang, L.; Hua, W. A Low-Complexity Three-Vector-Based Model Predictive Torque Control for SPMSM. *IEEE Trans. Power Electron.* **2021**, *36*, 13002–13012. [CrossRef]
25. Xu, Y.; Ding, X.; Wang, J.; Li, Y. Three-vector-based low-complexity model predictive current control with reduced steady-state current error for permanent magnet synchronous motor. *IET Electr. Power Appl.* **2020**, *14*, 305–315. [CrossRef]
26. Chen, R.; Shu, H.; Zhai, K. Low-Complexity Three-Vector Model Predictive Current Control with Fixed Switching Frequency for PMSM. In Proceedings of the CSEE, Winnipeg, MB, Canada, 1 June 2023. *early access*.
27. Li, X.; Tian, W.; Gao, X.; Yang, Q.; Kennel, R. A Generalized Observer-Based Robust Predictive Current Control Strategy for PMSM Drive System. *IEEE Trans. Ind. Electron.* **2022**, *69*, 1322–1332. [CrossRef]

28. Yu, K.; Wang, Z.; Hua, W.; Cheng, M. Robust Cascaded Deadbeat Predictive Control for Dual Three-Phase Variable-Flux PMSM Considering Intrinsic Delay in Speed Loop. *IEEE Trans. Ind. Electron.* **2022**, *69*, 12107–12118. [CrossRef]
29. Guo, T.; Wang, Z.; Zhang, H.; Jiang, X.; Tian, L. Cascaded predictive Speed Control Optimization Method based on Fuzzy Controller. In Proceedings of the 6th IEEE International Conference on Predictive Control of Electrical Drives and Power Electronics, PRECEDE 2021, Jinan, China, 20–22 November 2021; pp. 328–335.
30. Liu, J.; Ge, Z.; Wu, X.; Wu, G.; Xiao, S.; Huang, K. Predictive Current Control of Permanent Magnet Synchronous Motor Based on Duty-cycle Modulation. *Proc. CSEE* **2020**, *40*, 3319–3328.
31. Xiao, X.; Zhang, Y.; Wang, J.; Du, H. An Improved Model Predictive Control Scheme for the PWM Rectifier-Inverter System Based on Power-Balancing Mechanism. *IEEE Trans. Ind. Electron.* **2016**, *63*, 5197–5208. [CrossRef]
32. Han, Y.; Gong, C.; Yan, L.; Wen, H.; Wang, Y.; Shen, K. Multiobjective Finite Control Set Model Predictive Control Using Novel Delay Compensation Technique for PMSM. *IEEE Trans. Power Electron.* **2020**, *35*, 11193–11204. [CrossRef]